



HAL
open science

New lithostructural map of the Doropo region, northeast Côte d'Ivoire: Insight from structural and aeromagnetic data

Ziandjêdé Hervé Siagné, Tahar Aïfa, Alain Nicaise Kouamelan, N'Guessan Nestor Houssou, Wilfried Digbeu, Bi Koffi Fidèle Kakou, Pierrick Couderc

► **To cite this version:**

Ziandjêdé Hervé Siagné, Tahar Aïfa, Alain Nicaise Kouamelan, N'Guessan Nestor Houssou, Wilfried Digbeu, et al.. New lithostructural map of the Doropo region, northeast Côte d'Ivoire: Insight from structural and aeromagnetic data. *Journal of African Earth Sciences*, 2022, 196, pp.104680. 10.1016/j.jafrearsci.2022.104680 . insu-03751933

HAL Id: insu-03751933

<https://insu.hal.science/insu-03751933>

Submitted on 18 Aug 2022

HAL is a multi-disciplinary open access archive for the deposit and dissemination of scientific research documents, whether they are published or not. The documents may come from teaching and research institutions in France or abroad, or from public or private research centers.

L'archive ouverte pluridisciplinaire **HAL**, est destinée au dépôt et à la diffusion de documents scientifiques de niveau recherche, publiés ou non, émanant des établissements d'enseignement et de recherche français ou étrangers, des laboratoires publics ou privés.

New lithostructural map of the Doropo region, northeast Côte d'Ivoire: Insight from structural and aeromagnetic data

Ziandjêdé Hervé Siagné^{1,2}, Tahar Aïfa^{2,*}, Alain Nicaise Kouamelan¹, N'Guessan Nestor Houssou¹, Wilfried Digbeu¹, Bi Koffi Fidèle Kakou³, Pierrick Couderc³

¹UFR STRM, Université Félix Houphouët-Boigny, Abidjan-Cocody, 22 B.P. 582 Abidjan 22, Côte d'Ivoire

²Univ Rennes, Géosciences Rennes - CNRS UMR6118, Bat.15, Campus de Beaulieu, 35042 Rennes cedex, France

³Ampella-Centamin Mining Co., 20 BP 945 Abidjan 20, Côte d'Ivoire

*corresponding author: Tahar.aifa@univ-rennes1.fr

Abstract

This study, performed in the Doropo region (northeastern Côte d'Ivoire) in the Paleoproterozoic domain (southern part of the WAC), aims to produce a detailed lithostructural map of this area. The geology of this region is less known due to the thick lateritic overburden and the scarcity of outcrops. Recent airborne geophysical data (aeromagnetic) integrated with field structural and lithological observations allowed to distinguish several lithologies including biotite granite, gneissic and migmatitic granite, granodiorite, tonalite, gabbro, amphibolite, rhyolite and dolerite. Filtering techniques of derivatives, upward continuation, tilt, analytical signal, spectral analysis and 3D Euler deconvolution showed the presence of faults, shear zones and intrusions. The structural analysis revealed four deformation events (D₁-D₄): (i) D₁ is a N-S compression marked by E-W foliation (S₁), conjugate NE-SW and NW-SE sinistral and dextral shears, respectively, as well as F₁ folds with E-W axial planes; (ii) D₂ is a major transpressive phase characterized by an intense NE-SW foliation (S₂), E-W dextral shear zones, a weakly dipping stretching L₂ lineation plunging N-E, and NE-SW faults; (iii) D₃ is a NE-SW compressional phase generated NW-SE foliation (S₃) with ~E-W shears, and NW-SE axial plane F₃ folds; (iv) D₄ is a late, rather brittle phase characterized by brittle structures (faults, fractures, etc.) and the emplacement of NE-SW and NW-SE dolerite dykes. This tectonic evolution demonstrates that the Doropo region was subject to ductile and then brittle deformations. Furthermore, we suggest that the geodynamic model which could have prevailed in the Doropo region occurred in an oceanic arc collisional tectonic context.

Keywords: granitoids, dolerite dyke, fault, aeromagnetic, geodynamic model, structural analysis

1 **1. Introduction**

2 The Paleoproterozoic terrains of the West African Craton (WAC), particularly those of the
3 Man-Leo Shield, are composed of granitoid and greenstone belts (Metelka et al., 2011; Aïfa,
4 2021). They represent an interesting target for mineral exploration because they contain
5 numerous mineral deposits (Allibone et al., 2002; Feybesse et al., 2006; Béziat et al., 2008;
6 Amponsah et al., 2015, 2016; Markwitz et al., 2016; Goldfarb et al., 2017). Unfortunately, these
7 regions are very often characterized by surface weathering (lateritization) and limited outcrops
8 that can hinder cartographic surveying, mineral exploration and structural studies. The recourse
9 to use high resolution aeromagnetic data processing appears then as an essential tool to study
10 these terrains. Magnetism has shown its effectiveness in the study of similar terrains, especially
11 within the WAC by producing new geological data (Betts et al., 2003; Peschler et al., 2004;
12 Direen et al., 2005; Peschler et al., 2006; Agyei Duodu et al., 2009; Aitken and Betts, 2009;
13 Stewart and Betts, 2010; Metelka et al., 2011; Perrouy et al., 2012; Baratoux et al., 2015;
14 Eldosouky et al., 2017).

15 Thus, the recently acquired (2015) aeromagnetic data in the Doropo region (northeast Côte
16 d'Ivoire) present a unique opportunity to investigate this region where no significant geological
17 studies have been done. This region appears promising for mineral prospects, with the current
18 presence of several exploration companies (e.g., Ampella-Centamin Co). Based on this mining
19 interest, detailed geological studies have become a necessity, as most mineral deposits (e.g.,
20 gold) are structurally controlled (Mériaud et al., 2019; Murray et al., 2019; Tourigny et al.,
21 2019). Processing (horizontal derivatives, upward continuations and 3D Euler deconvolution,
22 etc.) and interpretation of aeromagnetic data combined with field observations were undertaken
23 in order to gain a better understanding of the lithostructural organization of the Doropo region.
24 This study will contribute to existing geological information on the WAC by: (1) establishing
25 both subsurface and outcrop scale structures, and various deformational episodes of such
26 structures; (2) relating Doropo deformational episode to other documented events of terrains
27 within the WAC, especially Burkina Faso and northwest Ghana, and (3) helping produce an
28 improved lithostructural map at a scale of 1: 50,000 for the Doropo region.

29

30 **2. Geological setting**

31 The WAC (Fig. 1) occupies most of West Africa with areas of generally low relief (Bessoles,
32 1977). It is a huge craton of approximately 4,500,000 km², formed by a set of largely granitized
33 peneplanar chains of Precambrian age (Bessoles, 1977). Two major composite orogenic
34 episodes have marked the ancient history of the WAC (Bessoles, 1977): the Liberian (2.9-2.5

1 Ga) and the Eburnean (2.5-1.6 Ga) at the end of which all the craton stabilized around 1.9 Ga
2 (Liégeois et al., 2005; Begg et al., 2009; de Waele et al., 2015; Aïfa and Merabet, 2021). The
3 WAC, which is covered in its central part by the Neoproterozoic to Devonian Taoudeni Basin,
4 consists of:

- 5 (i) the Reguibat Shield to the north occurring in two large areas (Archean and Birimian)
6 separated by the Zednès Fault;
- 7 (ii) the Kédougou-Kéniéba and Kayes Inliers to the southwest, formed exclusively of
8 Paleoproterozoic formations occurring in narrow volcanic belts and sedimentary basins which
9 are intruded by Eburnean granitoids (Ledru et al., 1991; Liégeois et al., 2005; Lambert-Smith
10 et al., 2016; Masurel et al., 2017; Dabo et al., 2018). To the west of these inliers, the WAC is
11 bordered by the Caledonian-Hercynian chain of the Mauritanides of Precambrian to the
12 Devonian age end;
- 13 (iii) the Man-Leo Shield to the south, covers a large region of the craton. This Shield, like that
14 of the Reguibat, is divided into two parts: (a) in the west, the Kénéma-Man domain of an
15 Archean age and (b) in the east, the Baoulé-Mossi domain of Paleoproterozoic age which would
16 be the extension of the Birimian formations of Kédougou-Kéniéba beneath the Neoproterozoic
17 formations of the Taoudeni Basin (Bassot and Vachette, 1984). These two areas are separated
18 by the N-S Sassandra fault (Kouamelan, 1996). The similarities existing in the geological
19 evolution of the WAC, the Guyana Shield and the small cratonic block of São Luis indicate that
20 these entities formed the same block before its “recent” dislocation (Ledru et al., 1994;
21 Vanderhaeghe et al., 1998; Nomade et al., 2003; Klein and Moura, 2008; Chardon et al., 2020).
22 The Kénéma-Man domain of the Man Shield is made up of Archean rocks (3.4-2.6 Ga)
23 recognized in the west of Côte d'Ivoire, Guinea, Sierra Leone and Liberia (Camil et al., 1983;
24 Kouamelan et al., 1997a,b; Thiéblemont, 2005; Koffi et al., 2020). It comprises granulitic
25 gneisses (3.05 Ga), charnockites (2.8 Ga), Tonalite-Trondhjemite-Granodiorite (TTGs,
26 between 3.6 and 3.0 Ga) and Banded Iron Formations (BIFs) (Kouamelan et al., 2015; Koffi et
27 al., 2020). The Paleoproterozoic domain, which spans between the Archean domain (Kénéma-
28 Man) in the west and the Volta Basin in the east is characterized by rocks with ages between
29 2.2 and 2.0 Ga (Caen-Vachette, 1986; Gasquet et al., 2003; Feybesse et al., 2006; Vidal et al.,
30 2009; Castaing et al., 2004; de Kock et al., 2011). The Paleoproterozoic (Birimian) terrains are
31 composed of metavolcanic and metasedimentary rocks bordered by large batholiths of TTGs;
32 all intruded by plutons of calc-alkaline and alkaline granites (Milési et al., 1989; Pouclet et al.,
33 2006; Hein, 2010; Baratoux et al., 2011; Perrouy et al., 2012; Block et al., 2016; Lebrun et al.,
34 2016; Masurel et al., 2017). These rocks can be linked to a multistage orogenic event: the

1 Eburnean (2.5-1.8 Ga; [Bonhomme, 1962](#); [Boher et al., 1992](#)). The beginning of the Eburnean
2 orogeny varies according to the regions: (i) in the northeast Baoulé-Mossi, it occurred around
3 2.16-2.15 Ga ([Baratoux et al., 2011](#); [Block et al., 2016](#)), (ii) in the southeast ([Feybesse et al.,](#)
4 [2006](#); [Perrouty et al., 2012](#)) and (iii) in the northwest ([Liégeois et al., 1991](#); [Egal et al., 2002](#);
5 [Lebrun et al., 2016](#) ; [Eglinger et al., 2017](#); [Masurel et al., 2017](#)), it is around 2.12 Ga. However
6 [de Kock et al. \(2011, 2012\)](#) have shown that the Eburnean comprises two stages: the
7 Eoeburnean orogenic cycle which captured the geological history between 2.5 Ga and ~2.140
8 Ga. This was followed with deposition of the sedimentary and volcanoclastic deposition and
9 syndepositional plutonism in the numerous basins separating the Eoeburnean crust due to
10 crustal extension. The Eburnean orogenic cycle commenced with the closure of these basins
11 and syntectonic granite emplacements from 2126 Ma onwards. Studies on the structural
12 evolution of the Birimian of the Man-Leo Shield have led to the recognition of a history
13 characterized by a complex polycyclic deformation linked to the Eburnean orogeny ([Milési et](#)
14 [al., 1986](#); [Ledru et al., 1989](#); [Feybesse et al., 2006](#); [Lompo, 2010](#); [Baratoux et al., 2011](#);
15 [Tshibubudze et al., 2013](#); [Block et al., 2016](#)). Thus, three major deformation phases (D₁, D₂ and
16 D₃) have been identified ([Milési et al., 1986](#); [Ledru et al., 1989](#); [Feybesse et al., 1989, 2006](#);
17 [Lompo, 2010](#); [Baratoux et al., 2011](#)). However, other deformation phases (D₄, D₅, D₆ and D₇)
18 are often observed but they are generally more local ([Vidal et al., 1996](#); [Block et al., 2016](#);
19 [McFarlane et al., 2019](#)). Some of these various deformation events are summarized in Table 1.
20 The study area belongs to the Paleoproterozoic domain of the Man-Leo Shield ([Fig. 2](#)). It is
21 located in the northeast of Côte d'Ivoire. Ampella-Centamin Co's cartographic exploration
22 work has highlighted Birimian units. These formations consist mainly of granitoids adjacent to
23 the southwestern limit of the Boromo Greenstone Belt and to the east by the Lawra Belt. [Block](#)
24 [et al. \(2015, 2016\)](#) suggest that these granitoid domains of northwest Ghana, precisely the
25 granitoid domain of "Bole Boulenga", can be linked to those of Côte d'Ivoire (Nassian granitoid
26 domain) and that both of these domains belong to the same geological province based on
27 geochemical and geochronology data. This confirms the already published research works in
28 the northeast of Côte d'Ivoire ([Arnould, 1961](#); [Delor et al., 1995](#); [Hirdes et al., 1996](#); [Lüdtke et](#)
29 [al., 1998](#); [Vidal et al., 2009](#); [Baratoux et al., 2015](#); [Block et al., 2015, 2016](#); [Siagné et al., 2021](#);
30 [Digbeu et al., 2022](#)). They represent a granito-gneissic basement intruded by various granites
31 and granodiorites intersected by pegmatitic and doleritic dykes. Furthermore, the structures in
32 the northeast of Côte d'Ivoire are similar to those in southwestern Burkina Faso rich in gold
33 indices (e.g., Napelepera, Batié; [Siagné et al., 2021](#)).

34

1 **3. Methodology**

2 Two major approaches (field and geophysical data analysis) were necessary to produce a
3 detailed map of the region. A field phase was used to collect lithological, structural and
4 magnetic susceptibility data followed by the processing of aeromagnetic data. All data acquired
5 (geophysical, lithological and structural) were integrated within a GIS software for
6 interpretation.

7 Field work resulted in:

- 8 - Identifying the different lithologies encountered, describing them macroscopically as well as
9 measuring their magnetic susceptibility using an SM30 field susceptibility-meter. The
10 macroscopic description focused on textural and mineralogical features.
- 11 - The structural framework was described by highlighting the structures that are manifestation
12 of deformations that have affected these different lithologies while specifying their direction
13 and dip if possible. Above all, by establishing their spatial, crosscutting relationships and
14 relative chronology between different deformation events. The various measurements
15 obtained were subsequently processed with the SpheriStat software in order to identify the
16 main directions.

17 The aeromagnetic data were acquired within the framework of the Doropo Project by the UTS
18 Geophysics company on behalf of Ampella-Centamin Mining in northeast Côte d'Ivoire. The
19 acquisition was made using a *Cessna Grand Caravan C208* type aircraft registered under ZS-
20 *ABN* and the aircraft was piloted by *Geotch Aviation Ltd.* A total of 21,589 km of lines were
21 flown. The flight lines were spaced at intervals of 200 m and 100 m (filling) in the direction
22 160°-340° while the control lines were spaced 2000 m and 1000 m (filling) in the direction
23 070°-250° at an average flight altitude of 100 m. The aeromagnetic data obtained underwent a
24 first processing by making specific corrections to be used and reliable for the further processing
25 ([Allard and Bois, 1999](#)). Diurnal, altitude, topography and latitude corrections were applied.
26 After that, the data from these corrections were gridded on a 25 m x 25 m cell size using Geosoft
27 Oasis Montaj software ([Finn and Anderson, 2015](#)). This allowed to obtain the total magnetic
28 intensity map on which several filters were applied in order to highlight the geological
29 properties ([Metelka et al., 2011](#); [Perrouy et al., 2012](#); [Santos et al., 2017](#); [Osinowo et al., 2020](#);
30 [Aïfa and Lo, 2021](#)). In this study, we used the data sets from the reduction to the pole, the
31 upward continuation, the vertical gradient along X, Y and Z, the analytic signal, the tilt
32 derivative, the spectral analysis and 3D Euler deconvolution. Shaded-relief technique has been
33 applied to all these different data set compilations to highlight anomalies.

1 The Fast Fourier Transform (FFT) algorithm has been applied to magnetic data for reduction to
 2 the pole (MacLeod et al., 1993; Li, 2008). Due to the low magnetic inclinations (e.g., $I = -5.9^\circ$,
 3 $D = -3.6^\circ$) and a field intensity of 32,704 nT in the centre of the study area, it was difficult to
 4 successfully reduce the magnetic data to the magnetic pole (RTP). Therefore, we used the
 5 pseudo-RTP technique (Luo et al., 2010). It consisted in reducing the magnetic field data to the
 6 equator. Thereafter, the data were subsequently reversed (i.e., multiplied by -1) to potentially
 7 mimic the RTP and position the peaks of the magnetic anomalies above their sources (Baranov
 8 and Naudy, 1964; Bhattacharya, 1966; Hildenbrand, 1983; Luo et al., 2010).

9 The upward continuation is a technique that highlights deep structures. It makes it possible to
 10 attenuate the anomalies as a function of wavelengths, the shorter the wavelength, the larger the
 11 attenuation (Blakely, 1996). For this study, upwards to 100 m, 200 m, 500 m and 1000 m were
 12 applied in order to highlight the deep structures on the RTP map.

13 The first derivatives filter applied to the RTP map was useful for the interpretation of structural
 14 discontinuities as it increases the contrasts between positive and negative anomalies, thus
 15 providing details on the limits of magnetic units. This helped to determine the contacts between
 16 the various structures or lithologies (Elkins, 1951; Hood, 1965; Cordell and Grauch, 1985;
 17 Blakely and Simpson, 1986; Grauch and Cordell, 1987).

18 The analytic signal (AS) and the tilt derivative are filters based on a three-dimensional
 19 combination of the residual magnetic field derivatives in three dimensions. The mathematical
 20 expression of the AS for a magnetic anomaly (M) in 3D is defined as being a complex vector
 21 which can be expressed as follows (Roest et al., 1992):

$$22 \quad |AS(x, y)| = \left[\left(\frac{\partial M}{\partial x} \right)^2 + \left(\frac{\partial M}{\partial y} \right)^2 + \left(\frac{\partial M}{\partial z} \right)^2 \right]^{1/2}$$

23 It is independent of the direction of magnetization and the direction of the Earth's magnetic
 24 field (Nabighian, 1974; Roest et al., 1992). This means that bodies with the same geometry
 25 have the same AS (Milligan and Gunn, 1997). In addition, the geological structures with strong
 26 magnetization can be better assessed in shape and dimension.

27 The tilt derivative used in this study, based on the tilt angle θ of a magnetic anomaly which is
 28 considered as local phase, can be expressed as a horizontal gradient $\frac{d\theta}{dh} = \frac{z}{x^2+z^2}$. At $x = 0$

29 one can get $z = \left(\frac{d\theta}{dh} \right)^{-1}$ which is useful to map the edges and depths of causative sources (e.g.,
 30 Salem et al., 2007, 2010). The application of such filters was made on the RTP map.

1 The power spectral analysis of the magnetic anomaly can also be used to estimate the depths
2 average of the various magnetic sources based on the space transformation of the magnetic data
3 into various frequency fields (Battacharyan, 1966; Spector and Grant, 1970). Spector and Grant
4 (1970) introduced a procedure to compute the depth at the top of the causative magnetic source
5 using the radial power spectrum. It has been further improved to calculate additionally the depth
6 of its centroid and its base (Bhattacharyya and Leu, 1975a,b, 1977; Okubo et al., 1985; Tanaka
7 et al., 1999).

8 Meanwhile Euler's deconvolution is a processing which allows estimating the position and the
9 depth of the magnetic sources from mesh data covering the survey area. This processing
10 requires the calculation of horizontal and vertical gradients.

11 The choice of the source model or the structural index, window size (Table 2), the exactitude
12 of the flight altitude and topographic surfaces, and the spacing of flight lines are important to
13 have reasonable and accurate results. The expression of Euler's equation is given by
14 (Thompson, 1982):

$$15 \quad (x - x_0) \frac{\partial \Delta T}{\partial x} + (y - y_0) \frac{\partial \Delta T}{\partial y} - (z - z_0) \frac{\partial \Delta T}{\partial z} = -N \Delta T(x, y)$$

16 where x, y, z denote local coordinates, x_0 , y_0 , z_0 the coordinates of the postulated source
17 location, ΔT the difference between the anomaly and the regional field, and N the structural
18 index (SI).

19 The remanent magnetization is negligible here and therefore does not affect the result of the
20 calculations (Allard and Bois, 1999; Reid et al., 1990). In this study, the parameters used for
21 the calculation of Euler solutions depths are: (i) a specific structural index $SI = 1$ for the
22 detection of dykes; (ii) a tolerance of the solution estimated at 15%. As the profiles are spaced
23 100 m apart, and the maps have been calculated with a 25 m x 25 m grid, the amount of data
24 has increased significantly. An evaluation of the Euler solutions depths on thin surfaces (0-50
25 m, 50-75 m, etc.) has been carried out. This has highlighted the obscured near to subsurface
26 structures.

27

28 **4. Results**

29 ***4.1. Facies and magnetic susceptibility***

30 Field observations complemented by drill core samples allowed to distinguish several
31 lithologies in the Doropo region. The different mineralogical proportions mentioned below are
32 based on a visual estimation. The main lithologies in order of abundance are:

1 (i) **Biotite granite** is the dominant lithology in the region and it is encountered all across the
2 study area. It may occur in massive or circular or dome or slab of extremely variable size (meter
3 to kilometer). It can also be observed as a cluster of large blocks exposed by erosion. The rock
4 is leucocratic to mesocratic and ranging from fine- to coarse-grained (Fig. 3a). Based on visual
5 estimation, the rock is mainly composed of quartz (~ 60%), feldspar (~30%), biotite (~10%)
6 and sometimes small euhedral crystal of sulphides. Histograms from magnetic susceptibility
7 (MS) measurements in the field and laboratory show a multimodal distribution, with MS values
8 in the ranges of $0.025 \times 10^{-3} - 17.1 \times 10^{-3} SI$ and $0.01 \times 10^{-3} - 12.1 \times 10^{-3} SI$ in the field and in
9 the laboratory, respectively (Figs. 4a, 5a, Table 3).

10 (ii) **Gneissic and migmatitic granites** are found in the south, east and north of the study area.
11 They appear as circular or large slabs and are cross-cut by several quartzo-feldspathic veins
12 (Fig. 3b) and contain mafic enclaves (Fig. 3c). They are light- to grey coloured, medium- to
13 coarse-grained, and show a gneissic texture defined by alternating light colour (quartz, feldspar)
14 and dark colour mineral (mica, amphibole) rich beds, which sometimes are migmatitic.
15 Furthermore, the rocks contain quartz (~55%), feldspar (~35%), biotite (~5%), and some rare
16 amphibole (~3%) and magnetite. Their histogram relatively displays high values and
17 substantially close to those of biotite granite. Magnetic susceptibility values range from
18 0.093×10^{-3} to $12.9 \times 10^{-3} SI$ and 0.55×10^{-3} to $9.98 \times 10^{-3} SI$ in the field and laboratory,
19 respectively (Figs. 4b, 5b).

20 (iii) **Granodiorite** are most often found in contact with or as enclaves within the biotite granite.
21 They occur as circular or slab or meter-size block, and are mesocratic, medium- to coarse-
22 grained (Fig. 3d). The rocks also show a granitic texture and contain feldspar (~60%), quartz
23 (~25%), amphibole (~10%), biotite (~5%) and accessory sulphide minerals. These rocks
24 sometimes show a weak foliation defined by aligned amphibole and biotite grains. Their
25 magnetic susceptibility (MS) is moderate with MS values in the ranges of $1.59 \times 10^{-3} -$
26 $7.73 \times 10^{-3} SI$ in the field and $0.07 \times 10^{-3} - 4.33 \times 10^{-3} SI$ in the laboratory (Figs. 4c, 5c).

27 (iv) **Gabbro** occurs in the shape of small decimeter-size nodules or as enclaves within the biotite
28 granite and is found in the northern part of the study area. The rock is melanocratic, medium-
29 to coarse-grained, and consists of feldspar (~70%), pyroxene (~25%), and rare amphibole (<
30 5%) (Fig. 3e). The rock is also cut by quartzofeldspathic veins (probably associated with the
31 rhyolite volcanism). The histograms show low to moderate magnetic susceptibility values (Figs.
32 4d, 5d). Magnetic susceptibility in the field and laboratory varies from ranges $0.22 \times 10^{-3} -$
33 $0.36 \times 10^{-3} SI$ to $0.03 \times 10^{-3} - 0.23 \times 10^{-3} SI$, respectively.

1 (v) *Amphibolite* generally occurs as enclaves within the biotite granite, gneissic and migmatitic
2 granites, granodiorite and tonalite. The rock is dark green, fine- to medium-grained, and is
3 crossed by numerous deformed thin quartz and feldspar veins (Fig. 3f). It is mainly composed
4 of amphibole (~80-70%) and feldspar (~30%). The observation of the histograms shows low to
5 medium magnetic susceptibility values (Figs. 4e, 5e). These magnetic susceptibility values vary
6 within the ranges $0.003 \times 10^{-3} - 0.97 \times 10^{-3} SI$ and $0.01 \times 10^{-3} - 0.35 \times 10^{-3} SI$, in the field
7 and laboratory, respectively.

8 (vi) *Rhyolite* is less represented in the study area and appears as small meter-size boulders or
9 dome-like outcrops in its central part. To the naked eye, the rock is light in colour, glassy, and
10 composed of quartz and feldspar phenocrysts and some disseminated pyrite crystals (Fig. 3g).
11 It is the only felsic volcanic unit encountered in the Doropo region and show no apparent
12 metamorphic alteration. The magnetic susceptibility displays a low value which varies from
13 0.009×10^{-3} to $1.5 \times 10^{-3} SI$ (Fig. 5f).

14 (vii) *Dolerite* is highlighted in the core samples and occurs as dykes (Fig. 3h). The rock is dark
15 to dark gray in colour, and is fine- to medium-grained. It contains feldspar (~50%), pyroxene
16 (~40-30%) and some calcite veins. The histogram shows very high susceptibility magnetic
17 above $26.1 \times 10^{-3} SI$ (Fig. 5g).

18

19 **4.2. Structural analysis**

20 The Doropo region was submitted to four deformation phases which are denoted as D₁, D₂, D₃
21 and D₄.

22 **4.2.1 D₁ Deformation phase**

23 D₁ deformation is observed in the gneissic granite in the Doropo, Gbatedjou, Bouko and Enioda
24 areas (Fig. 2). It is marked by an intense S₁ foliation generally oriented E-W with a moderate
25 to subvertical dip (40°-65°) towards the north (Fig. 6a). Following the S₁ foliation, F₁-folds are
26 identified and characterized by their open hinges whose axial planes has an E-W orientation
27 and axes plunging 40° to 45° towards the southwest (Fig. 6b). These F₁-folds are accompanied
28 by drag and intrafolial micro-folds which show both dextral and sinistral shears. NW-SE and
29 NE-SW to NNE-SSW oriented small-scale shear zones are also observed in the gneissic granite
30 (Fig. 6c-d). These shear zones translate a conjugated shear with dextral and sinistral play,
31 respectively. It should be noted that the NW-SE dextral shear is very important in the entire
32 study area. These different shear zones are also evidenced by sigmoid-shaped porphyroblasts.
33 All these field observations show that D₁ was an N-S oriented shortening event which has
34 produced the above mentioned structures.

1 **4.2.2 D₂ Deformation phase**

2 The structures related to the D₂ deformation has been observed in the field within the gneissic
3 granite of Bouko and the migmatitic granite of Danoa where it appears as an intense penetrative
4 S₂ foliation oriented NE-SW (Fig. 7a), and was folded by a later D₃ deformation event near
5 Bouko and Danoa. The dips of this S₂ foliation vary between 50° and 85° towards the northwest
6 at Bouko and Danoa. S₂ is marked by metamorphic differentiated alternating beds of quartz-
7 feldspar minerals, biotite and amphibole. It is also distinguished by a 040°-050° oriented
8 fracturing found in meter wide quartz veins at Enioda. This brittle feature may be presented as
9 thin open fractures without crystallization, which in places can be crosscut by a later NW-SE
10 oriented fracture set. This deformation phase is also distinguished by a stretching lineation (L₂)
11 observed in Bouko's gneissic granite which plunges 10° to 30° towards the northeast (Fig. 7b).
12 In the Bouko sector, the D₂ deformation is characterized by meter to decimeter thick dextral
13 shear zones oriented E-W with a subvertical dip (Fig. 7c). These shear zones are characterized
14 by sigmoid-shaped pods and S-C fabrics. Moreover, a N-S oriented shear zones has been found
15 in the Bouko sector as well as asymmetric intrafolial folds (F₂) in the gneissic granite. The D₂
16 deformation is also characterized by S-C fabrics reflecting sinistral ductile shear observed in
17 the Lagbo's migmatitic granite (Fig. 7d). D₂ is the most important phase in the region which
18 affected the granitoids. It is a NW-SE shortening phase responsible for the different structures
19 observed.

20 **4.2.3 D₃ Deformation phase**

21 D₃ structures can be observed in the migmatitic granites of Danoa and sometimes rarely in the
22 biotite granite of Kodo. D₃ deformation generated an intense S₃ foliation (Fig. 8a) generally
23 oriented NW-SE to NNW-SSW marked by a metamorphic differentiation of quartzo-
24 feldspathic and ferromagnesian (mainly biotite and amphibole) mineral bands. Leucosomes and
25 melanosomes are parallel to this S₃ foliation. The D₃ is also responsible for the E-W oriented
26 sinistral shear zones very often found at Lagbo and rarely at Bouko and Doropo (Fig. 8b). These
27 are small centimeter to decimeter bands, most often with microfolds and sigmoidal clasts. This
28 deformation is also responsible for the F₃ folds with an NW-SE axial plane observed at
29 Gbatedjou and Bouko (Fig. 8c). D₃ can be attributed to a NE-SW shortening phase responsible
30 for these different structures.

31 **4.2.4 D₄ Deformation phase**

32 This is the latest phase that affected the region's granitoids. It is recognized through conjugate
33 fractures and shear fractures which are mainly E-W and NNE-SSW oriented on the one hand.
34 On the other hand, quartz veins and pegmatite dykes are mainly NE-SW and E-W to NW-SE,

1 and NE-SW oriented, respectively (Fig. 9a-b). ENE-WSW and E-W oriented strike-slip faults
2 are also noted (Fig. 9c). All these structures have the particularity of crosscutting those of
3 previous deformations. In addition, some E-W oriented fractures located in the eastern part of
4 the study area are sometimes filled with chlorite or epidote or both (Fig. 9d).

6 **4.3. Aeromagnetic data**

7 ***Reduction to pole***

8 The application of the reduction to pole (RTP) filter to the dataset of the total magnetic field
9 (Fig. 10a), allowed to obtain the map of the reduced magnetic field to the pole (Fig. 10b) for
10 the study area. This map shows negative and positive anomalies with magnetic field values
11 between -58.50 nT and 50.39 nT. These anomalies make it possible to highlight two magnetic
12 domains which are:

- 13 - A first magnetic domain characterized by negative anomalies (An_1 - An_2) has been observed in
14 the far northeast, a portion of the west and in the centre of the study area. This anomaly is the
15 least representative of the study area;
- 16 - A second domain characterized by positive anomalies (Ap_1 - Ap_2), elongated NW-SE to E-W
17 trending, has been observed in the centre.

18 Figure 10b also highlights numerous linear structures, both strongly and weakly magnetic,
19 oriented NE-SW and NW-SE which crosscut all rock units of the study area.

20 ***Upward continuation***

21 The application of the upward continuation filter to the RTP map, allowed to qualitatively
22 analyze the distribution of the magnetic anomaly sources at different depth levels (100 m, 200
23 m, 500 m and 1000 m). This has helped to enhance the roots of deep magnetic sources. Thus,
24 upward continuation maps are obtained (Fig. 11) at 100 m, 200 m, 500 m and 1000 m.
25 Comparison with the map obtained in figure 10b shows changes in function of elevation.

26 The upward continuations to 100 m (Fig. 11a) and to 200 m (Fig. 11b) show only very slight
27 variations compared to figure 10b. Similarly, weak and strongly magnetic fields, with positive
28 anomalies but, also linear NE-SW and NW-SE strongly magnetic structures can be recognized.
29 The upward continuations at 500 m (Fig. 11c) and 1000 m (Fig. 11d) however show some
30 changes. In figures 11c-d, both the strongly magnetic sets and a new positive magnetic set (AP_3)
31 can be observed in the northwest of the map. In addition, elongations of these magnetic domains
32 are clearly visible with orientations towards the NW-SE (AP_2) and E-W (AP_1). One also notes
33 the disappearance of the linear NW-SE structures in favour of those oriented NE-SW (AP_3).

34 ***Gradients***

1 The particularity of these filters is to increase the contrasts between positive and negative
2 anomalies. This allows to obtain three directional derivative maps according to X, Y and Z (Fig.
3 12a-c). Unlike the previous maps (Figs. 10, 11), they show the presence of new linear anomalies
4 in addition to the existing ones. Indeed, figures 12a-c all show numerous linear and curvilinear
5 structures strongly to weakly magnetic oriented in several directions (Fig. 12d). These different
6 structures show NE-SW and NW-SE but also ENE-WSW to E-W preferential orientations.

7 *Spectral analysis*

8 The map of the analytical signal (AS) obtained from the application of the filter is represented
9 in figure 13. On this map, important structures oriented in general NE-SW and NW-SE can be
10 observed. They are possibly of the same nature since they have the same analytical signal
11 (Milligan and Gunn, 1997). One can also note a perfect correlation with the gradient maps (Fig.
12 12) where these structures have been identified.

13 The tilt derivative map exhibits fair linear and curvilinear features at the edges of structures
14 clearly showing their contours (Fig. 14). The signal/noise ratio is improved and most of the
15 structures observable on the derivative maps (Fig. 12) are better highlighted. Therefore, no
16 possible artefacts can be distinguished by comparison of both techniques. While the AS shows
17 structures which have the same geometry and the same nature, once again corroborating the
18 occurrence of the main massive bodies and linear structures (intrusions, faults/shears). The
19 observation of the power spectrum (Spector and Grant, 1970) revealed three depths of the
20 causative magnetic sources (Fig. 15). Generally, shallow depth of the sources, the maximum of
21 which is about 425 m can be noticed. It can be interpreted as the roof of the basement knowing
22 that the terrains are mainly composed of granitoids. The source of both depths estimated at 125
23 m and 55 m, respectively, can be interpreted as the potential causative source contacts of
24 intrusions, fractures, fault structures, etc. and their host rocks.

25 *Euler deconvolution*

26 Outcrops exhibiting the different rocks types are rare (see Fig. 2b) and therefore we only present
27 here the 3D Euler deconvolution solutions (3D-EDS) which concern the faults and dykes (Fig.
28 16). The 3D Euler deconvolution allowed to estimate the position and depth of the causative
29 magnetic sources. Thus, the maps established at increasing depths were drawn over intervals of
30 depths: (i) 50-75 m (Fig. 16a); (ii) 75-100 m (Fig. 16b); (iii) 150-200 m (Fig. 16c) and (iv) 300-
31 400 m (Fig. 16d). Figures 16a-b could be clearly distinguished from the other figures as they
32 show the NE-SW and NW-SE linear structures which can be interpreted as dykes or faults. This
33 confirms the observations on the derivative (Fig. 12) and on the analytical signal (Fig. 13) maps.
34 These structures are located at an average depth of 50 m to 200 m. In addition, from 200 to 250

1 m depths the structures begin to disappear, as shown in [figures 16c-d](#), this is why the processing
2 of the 3D-EDS ceased at 400 m. This is well corroborated by the depths of the sources given
3 by spectral analysis ([Fig. 15](#)).

4 5 **5. Discussion**

6 *5.1 Aeromagnetic data and field observations integration*

7 The combination of geophysical data and field observations made it possible to establish the
8 first lithostructural map of the Doropo region ([Fig. 17](#)). This region comprises several
9 lithologies which are largely dominated by granitoids such as biotite granite, gneissic and
10 migmatitic granites, granodiorite and tonalite. They generally have low or moderate to high
11 magnetic susceptibility values which vary from 0.01×10^{-3} to 17.1×10^{-3} SI. This could be
12 explained by their mineralogical composition in ferromagnesian minerals and/or oxides or due
13 to alteration. On the RTP and upward continuation maps, they display pseudo-circular to
14 elliptical shaped which are also elongated NW-SE to E-W. They also show weakly to strongly
15 foliation. According to these observations, the granitoid of the Doropo region could be linked
16 to the granitoid types described by [Baratoux et al. \(2011\)](#), [Metelka, et al. \(2011\)](#) and [Block et
17 al. \(2016\)](#) in northwestern Ghana and southern Burkina-Faso. Indeed, these authors subdivided
18 these granitoids based on their: (i) mineralogical composition, (ii) magnetic response, (iii)
19 geochemistry, (iv) age and (v) deformation which occurred during several magmatic events
20 (ME_1 , ME_2 , ME_3 , etc.). These different groups of granitoids are generally characterized by a
21 very pronounced foliation (ME_1 and ME_2), sometimes not deformed (ME_3), with generally (a)
22 elongated to irregular (ME_1), (b) circular to elliptical (ME_2) or (c) elliptical to sigmoidal (ME_3)
23 shapes.

24 In the presence of these granitoids, gabbro and amphibolites can be distinguished, which appear
25 as enclaves dispersed on outcrops, and show a low to moderate magnetic intensity. The dolerite
26 dykes mainly oriented NE-SW and NW-SE, were identified on aeromagnetic maps ([Figs. 12-
27 14](#)) by their strong and linear signal (e.g., [Jessell et al., 2015](#); [Baratoux et al., 2019](#)), and
28 confirmed in drill core samples. The rhyolite, never been documented in previous studies, was
29 highlighted in the field, this suggests a local volcanic activity within a dominant granitoid
30 domain. [de Kock et al. \(2011, 2012\)](#) has illustrated a crustal relaxation phase between the
31 Eoeburnean and Eburnean phases which could explain the rhyolitic volcanism present in the
32 Doropo area.

33 Furthermore, the presence of linear structures (mostly dykes, foliation, faults and shear zones)
34 oriented NE-SW and NW-SE, as well as E-W were observed at different scales: (i) in the field

1 with tectonic structures showing stretching lineation (L_2) in granites, (ii) on aeromagnetic maps
2 (derivatives including tilt derivatives, etc.), where curvilinear magnetic lineaments are observed
3 in the southwest, while they are linear and oriented E-W in the north and east of the map.
4 Together these findings show a good correlation between the structures observed in outcrops
5 and aeromagnetic maps.

6 ***5.2 Tectonic and geodynamic implication***

7 The Doropo region owes its structure to four deformation phases (D_1 , D_2 , D_3 and D_4) among
8 which D_1 to D_3 played a major role. All of these deformation events have affected the granitoid
9 terrains. The first deformation phase is characterized by a tectonic fabric obtained during
10 recrystallization and migmatization. This D_1 deformation phase having generated: (i) a E-W S_1
11 foliation, (ii) conjugate sinistral and dextral shear zones oriented NE-SW and NW-SE,
12 respectively and (iii) F_1 folds with plunging axis 45° towards the southwest. It is the result of a
13 N-S compression which is less expressed in the region. This deformation phase has been
14 reported in other areas of the Man-Leo Shield. It presents variations in terms of its manifestation
15 due to lithological competence and the resulting structures. In addition, elsewhere in the WAC,
16 D_1 has been distinguished by (i) major faults in Sefwi (Ghana), (ii) foliations and folds, (iii)
17 thrusting (Baratoux et al., 2011; Metelka et al., 2011; Perrouty et al., 2012; Amponsah et al.,
18 2015, 2016; Block et al., 2016; McFarlane et al., 2019; Nunoo et al., 2022), (iv) crenulation
19 cleavage (D_3 : Baratoux et al., 2011; D_4 : Baratoux et al., 2015). In the Doropo region this
20 crenulation cleavage was not observed. Block et al. (2016) interpreted this N-S shortening as
21 being at the origin of significant crustal thickening which caused partial crustal fusion in
22 northwestern Ghana.

23 This first deformation phase (D_1) is followed by a NW-SE transpressive phase (D_2) which is
24 the most important in the Doropo region. It is also recognized as one of the major phases at the
25 WAC scale: (i) Northwestern and Southwestern Ghana (Perrouty et al., 2012; Block et al., 2016;
26 Nunoo et al., 2016; McFarlane et al., 2019), (ii) Northeastern Côte d'Ivoire (Vidal et al., 1996;
27 Lüdtke et al., 1998, 1999), (iii) in Burkina-Faso (Baratoux et al., 2011; Metelka et al., 2011)
28 and (iv) in the Kédougou-Kéniéba Inlier (KKI) in Sénégal (Dabo and Aïfa, 2010, 2011; Dabo
29 et al., 2018). In our study area, it is distinguished by intense NE-SW oriented S_2 foliations,
30 intrafolial F_2 folds, mineral stretching L_2 lineations slightly sloping towards the northeast, NE-
31 SW oriented faults (highlighted on the aeromagnetic maps) plunging, and E-W shear zone.
32 These large scale NE-SW oriented faults are affected by a later NNW-SSE faults. Furthermore,
33 folding observed within granitoids could be explained by the deformation intensity which
34 prevailed in the Doropo region.

1 The D₂ deformation phase is followed by two late phases: D₃ and D₄. D₃ seems to be responsible
2 for the shear bands, micro-folds as well as the S₃ foliation present in the granitoids. It is related
3 to NE-SW compression, described as late by [Vidal et al. \(1996\)](#) and [Block et al. \(2016\)](#). For
4 these authors, it is a compression which is most often accompanied by brittle deformation and
5 NW-SE crenulation cleavage. The D₄ deformation phase is characterized by a set of brittle
6 structures and also the emplacement of the NE-SW and NW-SE dolerite dykes. These dykes
7 may have been emplaced along the large NE-SW and NW-SE oriented faults which were
8 reactivated during this deformation event ([Vidal et al., 1996](#); [Lüdtke et al., 1998, 1999](#);
9 [Baratoux et al., 2019](#)).

10 Previous studies carried out in the WAC have shown that its Paleoproterozoic geodynamic
11 history took place as a polycyclic event characterized by horizontal shortening leading to
12 thickening of the crust followed by transcurrent tectonics forming regional shear zones (e.g.,
13 [Milési et al., 1989](#); [Baratoux et al., 2011](#); [Block et al., 2016](#); [Grenholm et al., 2019](#); [McFarlane
14 et al., 2019](#)). The different deformation phases (D₁-D₄) defined by shortening and shearing in
15 the Doropo area are in accordance with this polycyclic evolution in the WAC. However, the
16 stress regime related to these different deformation phases varies from one zone to another
17 within the WAC. In addition, the scarcity of the stretching lineations and the absence of
18 crenulation cleavage could be explained by: (i) the initial grain size in the deformed lithology
19 as well as the intensity of the flattening ([Piazolo and Passchier, 2002](#); [Baratoux et al., 2011](#);
20 [Teha, 2019](#)) and (ii) the competence of granitoids during the main deformation event.

21 The geodynamic evolution of the WAC is still a matter of debate. Some authors argue that
22 during the Eburnean, the tectonic regime that prevailed was dominated by vertical movements
23 and “dome and basin” structures ([Caby et al., 2000](#); [Pouclet et al., 2006](#); [Vidal et al., 2009](#);
24 [Lompo, 2010](#)). This tectonic regime is considered to be dominant during the Archean, and even
25 during the Lower Proterozoic ([Kouamelan et al., 1997b](#)). Another group of authors rather
26 attribute Eburnean events to a regime similar to that of plate tectonics, involving collisions
27 ([Feybesse and Milési, 1994](#); [Feybesse et al., 2006](#)). This argument is supported by [Baratoux et
28 al. \(2011, 2015\)](#) who proposed an assemblage of two eastern and western blocks in the Boromo
29 Belt (western Burkina-Faso). This amalgamation was initiated during an early N-S to NE-SW
30 shortening phase, well materialized in the eastern domain and absent in the western domain. It
31 probably corresponds to D₁ deformation phase and is a matter of debate. [Grenholm et al. \(2019\)](#)
32 go further by proposing a chronology of the main deformation events that affected the Birimian
33 crust during this collision phase. They proposed an early collisional phase, dated between 2.16
34 Ga and 2.12 Ga, characterized by compressional events both N-S and E-W oriented, and another

1 phase between 2.12 Ga and 2.07 Ga dominated by NW-SE oriented regional compression. All
2 these phases are responsible for the foliations, shear zones, faults, folds and thrusts that affected
3 the lithologies encountered in the Man Shield.

4 Structural data in the Doropo region show an area dominated by a transcurrent displacement
5 characterized by a 10°-30° NE-plunging stretching lineation during the NW-SE regional
6 compressional phase. These observations differ from vertical tectonics theory where
7 deformation patterns observed in the field do not match. Based on all these considerations, the
8 geodynamic model that could have prevailed in the Doropo region occurred in a collisional
9 tectonic context. During collisional phase, D₁ deformation would have occurred during the
10 Eoeburnean phase around 2.16-2.12 Ga along with a N-S compressional event, in an oceanic
11 arc context (Baratoux et al., 2015; Block et al., 2016). Further, (D₂-D₄) deformation phases took
12 place during the Eburnean phase after 2.12 Ga with a prevailing compressional event oriented
13 NW-SE (D₂), based on the geochronological results of Grenholm et al. (2019). The following
14 tectonic model can be suggested for the Doropo region: (i) a crustal thickening followed by
15 emplacement of granitoids in a magmatic arc context during the D₁ compressional phase (2.16-
16 2.12 Ga) (Fig. 18a), (ii) major shears and transcurrent faults occurred during the D₂
17 transpressional phase (2.12-2.07 Ga) (Fig. 18b) and finally (iii) a normal-transpressive
18 reactivation of the faults by dolerite dykes after 2.07 Ga and late granitic intrusions (Fig. 18c).

19

20 **6. Conclusion**

21 The geological investigations in the Doropo area have generated new lithological and structural
22 data for the northeastern part of Côte d'Ivoire. A new interpretative lithostructural map of the
23 region at 1:50,000 has been produced by coupling the aeromagnetic data to the field
24 observations.

25 Magnetic susceptibility measurements and the field observations complemented by drill core
26 samples made it possible to distinguish the following lithologies: (i) biotite granite, gneissic
27 and migmatitic granites, granodiorite and tonalite; (ii) gabbro, amphibolite and dolerite; and
28 (iii) rhyolite. All these lithologies were crosscut by pegmatites and quartz veins. Based on
29 adequate filtering on the aeromagnetic maps, the different limits of these formations could be
30 drawn. The spectral analysis and 3D Euler deconvolution maps helped in localizing and
31 estimating the depth of the causative sources of the major structures (faults, intrusions) between
32 50 m and 200 m.

33 The Doropo region was deformed by four tectonic phases: (i) N-S compressional phase (D₁)
34 characterized by an E-W foliation (S₁), conjugate dextral (NW-SE) and sinistral (NE-SW) shear

1 zones, and as well as F_1 folds with an E-W axial plane; (ii) most prominent NW-SE
2 transpressional phase (D_2) responsible for the regional NE-SW foliation (S_2), slightly steep
3 stretching L_2 lineation plunging towards the northeast, NE-SW faults, and E-W dextral shear
4 zones; (iii) NE-SW compressional phase (D_3) marked by NW-SE foliation (S_3), NW-SE axial
5 plane F_3 folds, and E-W sinistral shears, and finally (iv) late phase (D_4), responsible for brittle
6 structures (faults, fractures, etc.) and also the emplacement of NE-SW and NW-SE dolerite
7 dykes that intersecting all the lithologies of the region. These different deformation events
8 suggest that the geodynamic model that has prevailed in the Doropo region was due to
9 collisional tectonics. These new geological data are a contribution to previous studies in
10 northeastern Côte d'Ivoire where no detailed geological study has been carried out for several
11 decades. With the previous studies carried out in the neighboring regions of Ghana and Burkina
12 Faso, they contribute to a better understanding of the WAC geodynamics.

13

14 **Acknowledgements**

15 We would like to thank the Managing Director of Ampella-Centamin Co. (Côte d'Ivoire) for
16 providing us with the airborne data. This project, funded by Ampella-Centamin Co., also
17 received funding from the West African Economic and Monetary Union (UEMOA) through its
18 "Support Program for Training and the Research for Excellence 2019-2020 Edition". We thank
19 Dr. Koffi Raoul Teha and Dr. Yao Augustin Koffi for their help during structural data analysis.
20 Many thanks to Dr. Luc Siebenaller, Dr. Samuel Nunoo and the anonymous reviewers for their
21 invaluable comments and suggestions which helped to improve the quality of this paper. The
22 ZHS doctoral fellowship at Géosciences Rennes (France) was funded by the Ministry of Higher
23 Education and Scientific Research of Côte d'Ivoire. This is a contribution to the Unesco-
24 igcp638 program.

25

26 **References**

27 Agyei Duodu, J., Loh, G.K., Hirdes, W., Boamah, K.O., Baba, M., Anokwa, Y.M., Asare, C.,
28 Brakohiapa, E., Mensah, R.B., Okla, R., Toloczyki, M., Davis, D.W., Glück, S., 2009.
29 Geological map of Ghana 1:1,000,000. BGS/GGS, Accra (Ghana)/ Hannover (Germany).
30 Aïfa, T., 2021. Mineralization and sustainable development in the West African Craton: from
31 field observations to modelling. *Geological Society of London, Special Publications*, 502, 1-
32 29.

- 1 Aïfa, T., Lo, K., 2021. Aeromagnetic modelling of Precambrian subsurface structures of the
2 Tasiast area, NW Mauritania. *Geological Society of London, Special Publications*, 502,
3 309-329.
- 4 Aïfa, T., Merabet, N.E., 2021. Rock magnetic study on the Yetti-Eglab intrusions, Sahara:
5 Contribution to the West African Craton geology. *Geological Society of London, Special*
6 *Publications*, 502, 159-189.
- 7 Aitken, A.R.A., Betts, P.G., 2009. Constraints on the Proterozoic supercontinent cycle from the
8 structural evolution of the south-central Musgrave Province, central Australia. *Precambrian*
9 *Research*, 168, 284-300.
- 10 Allard M., Bois D., 1999. La géophysique appliquée à l'exploration minérale. Dans la
11 magnétométrie et la radiométrie. *Centre collégial de développement de matériel didactique*
12 (CCDM), Montréal (Québec), 161-311.
- 13 Allibone, A.H., McCuaig, T.C., Harris, D., Etheridge, M., Munroe, S., Byrne, D., Amanor, J.,
14 Gyapong, W., 2002. Structural controls on gold mineralization at the Ashanti Gold Deposit,
15 Obuasi, Ghana. *Society of Economic Geologists, Special Publications*, 9, 65-93.
- 16 Amponsah, P.O., Salvi, S., Beziat, D., Jessell, M.W., Siebenaller, L., Baratoux, L., 2015.
17 Geology and geochemistry of the shear-hosted Julie deposit, NW Ghana. *Journal of African*
18 *Earth Sciences*, 112, 505-523.
- 19 Amponsah, P.O., Salvi, S., Béziat, D., Baratoux, L., Siebenaller, L., Nude, P.M., Nyarko, R.S.,
20 Jessell, M.W., 2016. The Bepkong gold deposit, Northwestern Ghana. *Ore Geology Review*,
21 78, 718-723.
- 22 Arnould M., 1961. Etude géologique des migmatites et des granites précambriens du Nord-Est
23 de la Côte d'Ivoire et de la Haute-Volta méridionale. *Direction de la Prospection Minière*,
24 *Abidjan, Bulletin n° 1*, 175p.
- 25 Baranov, V., Naudy, H., 1964. Numerical calculation of the formula of reduction to the
26 magnetic pole. *Geophysics*, 29, 67-79.
- 27 Baratoux, L., Metelka, V., Naba, S., Jessell, M.W., Gregoire, M., Ganne, J., 2011. Juvenile
28 Paleoproterozoic crust evolution during the Eburnean orogeny (2.2-2.0 Ga), western Burkina
29 Faso. *Precambrian Research*, 191, 18-45.
- 30 Baratoux, L., Metelka, V., Naba, S., Ouyi, P., Siebenaller, L., Jessell, M.W., Nare, A., Salvi,
31 S., Beziat, D., Franceschi, G., 2015. Tectonic evolution of the Gaoua region, Burkina Faso:
32 Implications for mineralization. *Journal of African Earth Sciences*, 112, 419-439.
- 33 Baratoux, L., Soderlund, U., Ernst, R.E., de Roeber, E., Jessell, M.W., Kamo, S., Naba, S.,
34 Perrouy, S., Metelka, V., Yatte, D., Grenholm, M., Diallo, D.P., Ndiaye, P.M., Dioh, E.,

- 1 Cournède, C., Benoit, M., Baratoux, D., Youbi, N., Rouse, S., Bendaoud, A., 2019. New
2 U-Pb baddeleyite ages of mafic dyke swarms of the West African and Amazonian Cratons:
3 implication for their configuration in supercontinents through time. In: Srivastava, R.K.,
4 Ernst, R.E., Peng, P. (eds.) *Dyke Swarms of the World: A Modern Perspective*. Springer
5 *Geology*, 263-314. doi:10.1007/978-981-13-1666-1_7.
- 6 Bassot, J.P., Caen-Vachette, M., 1984. Données géochronologiques et géochimiques nouvelles
7 sur les granitoïdes de l'Est Sénégal : implications sur l'histoire du Birrimien de cette région.
8 In : Klerkx, J. and Michot, J. (editors), "*Géologie africaine*", Tervuren, 191-209.
- 9 Bessoles, B., 1977. Géologie de l'Afrique; le craton ouest africain. *Mémoire BRGM, n°88*,
10 *Orléans (France)*, 402p.
- 11 Begg, G.C., Griffin, W.L., Natapov, L.M., O'Reilly, S.Y., Grand, S.P., O'Neill, C.J., Hron-sky,
12 J.M.A., Poudjom Djomani, Y., Swain, C.J., Deen, T., Bowden, P., 2009. The lithospheric
13 architecture of Africa: seismic tomography, mantle petrology, and tectonic evolution.
14 *Geosphere*, 5(1), 23-50.
- 15 Betts, P.G., Valenta, R.K., Finlay, J., 2003. Evolution of the Mount Woods inlier, northern
16 Gawler Craton, Southern Australia: an integrated structural and aeromagnetic analysis.
17 *Tectonophysics*, 366, 83-111.
- 18 Béziat, D., Dubois, M., Debat, P., Nikiéma, S., Salvi, S., Tollon, F., 2008. Gold metallogeny in
19 the Birimian craton of Burkina Faso (West Africa). *Journal of African Earth Sciences*, 50,
20 215-233.
- 21 Bhattacharyya, B.K., 1966. Continuous spectrum of the total-magnetic-field anomaly due to a
22 rectangular prismatic body. *Geophysics*, 31(1), 97-121.
- 23 Bhattacharyya, B.K., Leu, L.K., 1975a. Spectral analysis of gravity and magnetic anomalies
24 due to a two-dimensional structure. *Geophysics*, 40, 993-1013.
- 25 Bhattacharyya, B.K., Leu, L.K., 1975b. Analysis of magnetic anomalies over Yellowstone
26 National Park: mapping of Curie point isothermal surface for geothermal reconnaissance.
27 *Journal of Geophysical Research*, 80, 4461-4465.
- 28 Bhattacharyya, B.K., Leu, L.K., 1977. Spectral analysis of gravity and magnetic anomalies due
29 to rectangular prismatic bodies. *Geophysics*, 42, 1, 41-50.
- 30 Blakely, R., Simpson, R., 1986. Approximating edges of source bodies from magnetic or
31 gravity anomalies. *Geophysics*, 51(7), 1494-1498.
- 32 Blakely, R.J., 1996. Potential theory in gravity and magnetic applications. *Cambridge*
33 *University Press*, 190p.

- 1 Block, S., Ganne, J., Baratoux, L., Zeh, A., Parra-Avila, L. A., Jessell, M. W., Ailleres, L.,
2 Siebenaller, L., 2015. Petrological and geochronological constraints on lower crust
3 exhumation during Paleoproterozoic (Eburnean) orogeny, NW Ghana, West African Craton.
4 *Journal of Metamorphic Geology*, 33(5), 463-494.
- 5 Block, S., Jessell, M., Ailleres, L., Baratoux, L., Bruguier, O., Zeh, A., Bosch, D., Caby, R.,
6 Mensah, E., 2016. Lower crust exhumation during Paleoproterozoic (Eburnean) orogeny,
7 NW Ghana, West African Craton: interplay of coeval contractional deformation and
8 extensional gravitational collapse. *Precambrian Research*, 274, 82-109.
- 9 Boher, M., Abouchami, W., Michard, A., Albarede, F., Arndt, N.T., 1992. Crustal growth in
10 West Africa at 2.1 Ga. *Journal of Geophysical Research*, 97, 345-369.
- 11 Bonhomme, M., 1962. Contribution à l'étude géochronologique de la plate-forme de l'Ouest
12 africain. *Annales de la Faculté des Sciences Université Clermont-Ferrand*, Géologie et
13 Minéralogie, 5, 62p.
- 14 Caby, R., Delor, C., Agoh, O., 2000. Lithologie, structure et métamorphisme des formations
15 birimiennes dans la région d'Odienné (Côte d'Ivoire) : rôle majeur du diapirisme des plutons
16 et des décrochements en bordure du craton de Man. *Journal of African Earth Sciences*, 30,
17 351-374.
- 18 Caen-Vachette, M., 1986. Apport de la géochronologie isotopique à la connaissance du
19 Protérozoïque Inférieur de l'Afrique de l'Ouest. *Publication CIFEG*, 1986/10. *Les formations*
20 *birimiennes en Afrique de l'Ouest*, 17-23.
- 21 Camil, J., Tempier, P., Pin, C., 1983. Ages libérien des quartzites à magnétite de la région de
22 Man (Côte d'Ivoire) et leur place dans l'orogénèse libérienne. *Comptes Rendus de*
23 *l'Académie des Sciences de Paris*, 296, 149-151.
- 24 Castaing, C., Thiéblemont, D., Chèvremont, P., Donzeau, M., Egal, E., Guerrot, C., Koté, S.,
25 Ouédraogo, I., Cocherie, A., Le Métour, J., 2004. Paleoproterozoic crustal evolution in
26 Burkina Faso (West African craton). *IGC 32nd International Geological Congress, Florence,*
27 *Italie*, 20-28/08/2004.
- 28 Chardon, D., Bamba, O., Traoré, K., 2020. Eburnean deformation pattern of Burkina Faso and
29 the tectonic significance of shear zones in the West African craton. *Bulletin de la Société*
30 *Géologique de France*, 191, <https://doi.org/10.1051/bsgf/2020001>.
- 31 Cordell, L., Grauch, V.J.S., 1985. Mapping basement magnetization zones from aeromagnetic
32 data in the San Juan Basin, New Mexico. In: Hinze, W.J., Ed., *The utility of regional gravity*
33 *and magnetic anomaly maps. Society of Exploration Geophysicists*, 181-197. doi:
34 10.1190/1.0931830346.ch16.

- 1 Dabo, M., Aïfa, T., 2010. Structural Styles and Tectonic evolution of the Kolia-Boboti
2 sedimentary basin, Kédougou-Kéniéba inlier, Eastern Senegal. *Comptes Rendus*
3 *Geoscience*, 342, 796-805, doi:10.1016/j.crte.2010.06.002.
- 4 Dabo, M., Aïfa, T., 2011. Late Eburnean deformation in the Kolia-Boboti sedimentary basin,
5 Kédougou-Kéniéba Inlier, Sénégal. *Journal of African Earth Sciences*, 60, 106-116,
6 doi:10.1016/j.jafrearsci.2011.02.005.
- 7 Dabo, M., Aïfa, T., Gassama, I., Ngom, P.M., 2018. Thrust to transpression and transtension
8 tectonics during the Paleoproterozoic evolution of the Birimian Greenstone Belt of Mako,
9 Kédougou-Kéniéba Inlier, Eastern Senegal. *Journal of African Earth Sciences*, 148, 14-29,
10 doi: 10.1016/j.jafrearsci.2018.05.010.
- 11 Delor, C., Siméon, Y., Vidal, M., Zéadé, Z., Koné, Y., Adou, M., Dibouahi, J., Bi-Irié, D., Yao,
12 B.D., N'Da, D., Pouclet, A., Konan, G., Diaby, I., Chiron, J.C., Dommanget, A., Kouamelan,
13 A., Peucat, J.J., Cocherie, A., Cautru, J.P. 1995. Carte géologique de la Côte d'Ivoire
14 1/200000, feuille de Nassian. *Ministère des Mines et de l'Energie. DMG, Abidjan, Côte*
15 *d'Ivoire*.
- 16 de Kock, G.S., Armstrong, R.A., Siegfried, H.P., Thomas, E., 2011. Geochronology of the
17 Birim supergroup of the West African craton in the Wa-Bole region of west-central Ghana:
18 Implications for the strathigraphic framework. *Journal of African Earth Sciences*, 59, 1-40.
- 19 de Kock, G.S., Théveniaut, H., Botha, P.M.W., Gyapong, W., 2012. Timing the structural
20 events in the Paleoproterozoic Bole-Nangodi belt terrane and adjacent Maluwe basin, West
21 African craton, in central-west Ghana. *Journal of African Earth Sciences*, 65, 1-24.
- 22 de Waele, B., Lacorde, M., Vergara, F., Chan, G., 2015. New insights on Proterozoic tectonics
23 and sedimentation along the peri-Gondwanan West African margin based on zircon U-Pb
24 SHRIMP geochronology. *Precambrian Research*, 259, 156-175.
- 25 Digbeu, W., Kouamelan, A.N., Tshibubudze, A., Siagné, Z.H., Kouadio, F.J.L.H., 2022.
26 Geochemistry of Mafic Rocks from the Birimian Basement of Doropo (Northeast of Côte
27 d'Ivoire): Petrogenetic and Geodynamic Implications. *Open Journal of Geology*, 12(6), 504-
28 520.
- 29 Direen, N.G., Cadd, A.G., Lyons, P., Teasdale, J.P., 2005. Architecture of Proterozoic shear
30 zones in the Christie Domain, western Gawler Craton, Australia: Geophysical appraisal of a
31 poorly exposed orogenic terra terrane. *Precambrian Research*, 142, 28-44.
- 32 Egal, E., Thiéblemont, D., Lahondère, D., Guerrot, C., Costea, C.A., Iliescu, D., Delor, C.,
33 Goujou, J.-C., Lafon, J.M., Tegye, M., Diaby, S., Kolié, P., 2002. Late Eburnean

1 granitization and tectonics along the western and northwestern margin of the Archean
2 Kenema-Man domain (Guinea, West African Craton). *Precambrian Research*, 117, 57-84.

3 Eglinger, A., Thébaud, N., Zeh, A., Davis, J., Miller, J., Parra-Avila, L.A., Loucks, R.,
4 McCuaig, C., Belousova, E., 2017. New insights into the crustal growth of the
5 Paleoproterozoic margin of the Archean Kénéma-Man domain, West African craton
6 (Guinea): Implications for gold mineral system. *Precambrian Research*, 292, 258-289.

7 Eldosouky, A.M., Abdelkareem, M., Elkhateeb, S.O., 2017. Integration of remote sensing and
8 aeromagnetic data for mapping structural features and hydrothermal alteration zones in Wadi
9 Allaqi area, South Eastern Desert of Egypt. *Journal of African Earth Sciences*, 130, 28-37.

10 Elkins, T.A., 1951. The second derivative method of gravity interpretation. *Geophysics*, 16(1),
11 29-50.

12 Feybesse, J.L., Milési, J.P., Johan, V., Dommange, A., Calvez, J.Y., Boher, M., Abouchami,
13 W., 1989. La limite Archéen-Protérozoïque inférieur de l'Afrique de l'Ouest: une zone de
14 chevauchement majeur antérieure à l'accident de Sassandra: l'exemple des régions
15 d'Odienné et de Touba (Côte d'Ivoire). *Comptes Rendus de l'Académie des Sciences, Paris*,
16 309, 1847-1853.

17 Feybesse, J.-L., Milési, J.-P., 1994. The Archean/Paleoproterozoic contact zone in West Africa:
18 a mountain belt of decollement thrusting and folding on a continental margin related to 2.1
19 Ga convergence of Archean cratons? *Precambrian Research*, 69, 199-227.

20 Feybesse, J.-L., Billa, M., Guerrot, C., Duguey, E., Lescuyer, J.-L., Milesi, J.-P., and Bouchot,
21 V., 2006. The Paleoproterozoic Ghanaian province: Geodynamic model and ore controls,
22 including regional stress modeling. *Precambrian Research*, 149, 149-196.

23 Finn, C.A., Anderson, E.D., 2015. Synthesis of geophysical data (phase V, deliverable 55).
24 Chapter B of Taylor, C.D. (ed.), Second projet de renforcement institutionnel du secteur
25 minier de la République Islamique de Mauritanie (PRISM-II). *United States Geological*
26 *Survey Open-File Report 2013-1280-B*, 60p.

27 Gasquet, D., Barbey, P., Adou, M., Paquette, J.L., 2003. Structure, Sr–Nd isotope geochemistry
28 and zircon U–Pb geochronology of the granitoids of Dabakala area (Côte d'Ivoire): evidence
29 for a 2.3 Ga crustal growth event in the Palaeoproterozoic of West Africa? *Precambrian*
30 *Research*, 127, 329-354.

31 Goldfarb, R.J., André-Mayer, A-S., Jowitt, S.M., Mudd, G.M., 2017. West Africa: The World's
32 Premier Paleoproterozoic Gold Province. *Economic Geology*, 112(1), 123-143.
33 doi:10.2113/econgeo.112.1.123

1 Grauch, V.J.S., Cordell, L., 1987. Limitations of determining density or magnetic boundaries
2 from the horizontal gradient of gravity or pseudogravity data. *Geophysics*, 52, 118-121.

3 Grenholm, M., Jessell, M., Thébaud, N., 2019. A geodynamic model for the Paleoproterozoic
4 (ca. 2.27-1.96 Ga) Birimian Orogen of the southern West African Craton: Insights into an
5 evolving accretionary-collisional orogenic system. *Earth-Science Reviews*, 192, 138-193.

6 Hein, K.A.A., 2010. Succession of structural events in the Goren greenstone belt (Burkina
7 Faso): Implications for West African tectonics. *Journal of African Earth Sciences*, 56, 83-
8 94.

9 Hildenbrand, T.G., 1983. FFTFIL: A filtering program based on two-dimensional Fourier
10 analysis: *United States Geological Survey Open-File Report 83-237*, 29p.

11 Hirdes, W., Davis, D.W., Lüdtke, G., Konan, K.G., 1996. Two generations of Birimian
12 (Paleoproterozoic) volcanic belts in northeastern Côte d'Ivoire (West Africa): consequences
13 for the "Birimian controversy". *Precambrian Research*, 80, 173-191.

14 Hood, P., 1965. Gradient measurement in aeromagnetic surveying. *Geophysics*, 30, 891-902.

15 Jessell, M.W., Santoul, J., Baratoux, L., Youbi, N., Ernst, R.E., Metelka, V., Miller, J., Perrouty,
16 S., 2015. An updated map of West African mafic dykes. *Journal of African Earth Sciences*,
17 112, 440-450.

18 Klein, E., Moura, C., 2008. São Luís craton and Gurupi belt (Brazil): possible links with the
19 West African Craton and surrounding pan-African belts. *Geological Society of London*,
20 *Special Publications*, 294(1), 137-151.

21 Koffi, G.R.S., Kouamelan, A.N., Allialy, M.E., Coulibaly, Y., Peucat, J.J., 2020. Re-evaluation
22 of Leonian and Liberian events in the geodynamical evolution of the Man-Leo Shield (West
23 African Craton). *Precambrian Research*, 338, 105582.

24 Kouamelan, A.N., 1996. Géochronologie et géochimie des formations archéennes et
25 protérozoïques de la dorsale de Man en Côte d'Ivoire, implication pour la transition archéen-
26 protérozoïque. *Thèse de Doctorat*, Université de Rennes 1, France, pp. 1-227.

27 Kouamelan, A.N., Peucat, J.J., Delor, C., 1997a. Reliques archéennes (3.15 Ga) au sein du
28 magmatisme Birimien (2.1 Ga) de Côte d'Ivoire, craton Ouest-Africain. *Comptes Rendus de*
29 *l'Académie des Sciences*, Paris, 324, 719-727.

30 Kouamelan, A.N., Delor, C., Peucat, J.J., 1997b. Geochronological evidence for reworking of
31 Archean terrains during the Early Proterozoic (2.1 Ga) in the western Côte d'Ivoire (Man
32 Rise – West African Craton). *Precambrian Research*, 86, 177-199.

33 Kouamelan, A.N., Djro, S.C., Allialy, M.E., Paquette, J.L., Peucat, J.J., 2015. The oldest rock
34 of Ivory Coast. *Journal of African Earth Sciences*, 103, 65-70.

- 1 Lambert-Smith, J.S., Lawrence, D.M., Muller, W., Treloar, P.J., 2016. Palaeotectonic setting
2 of the south-eastern Kedougou-Kenieba Inlier, West Africa: New insights from igneous trace
3 element geochemistry and U-Pb zircon ages. *Precambrian Research*, 274, 110-135.
- 4 Lebrun, E., Thébaud, N., Miller, J., Ulrich, S., Bourget, J., Terblanche, O., 2016.
5 Geochronology and lithostratigraphy of the Sigui district: Implications for gold
6 mineralisation in the Sigui Basin (Guinea, West Africa). *Precambrian Research*, 274, 136-
7 160.
- 8 Ledru, P., Milési, J.-P., Feybesse, J.-L., Dommange, A., Johan, V., Diallo, M., Vinchon, C.,
9 1989. Tectonique transcurrente et évolution polycyclique dans le Birimien, Protérozoïque
10 inférieur du Sénégal-Mali (Afrique de l'Ouest). *Comptes Rendus de l'Académie des
11 Sciences*, Paris, 308, 117-122.
- 12 Ledru, P., Pons, J., Milesi, J.P., Feybesse, J.L., Johan, V., 1991. Transcurrent tectonics and
13 polycyclic evolution in the lower Proterozoic of Senegal-Mali. *Precambrian Research*, 50,
14 337-354.
- 15 Ledru, P., Johan, V., Milesi, J.P., Tegye, M., 1994. Markers of the last stages of the
16 Paleoproterozoic collision: evidence for a 2 Ga continent involving circum-South Atlantic
17 provinces. *Precambrian Research*, 69, 169-191.
- 18 Li, X., 2008. Magnetic reduction-to-the-pole at low latitudes: Observations and considerations.
19 *The Leading Edge*, 27, 990-1002.
- 20 Liégeois, J.P., Claessens, W., Camara, D., Klerkx, J., 1991. Short-lived Eburnian orogeny in
21 southern Mali. Geology, tectonics, U-Pb and Rb-Sr geochronology. *Precambrian Research*,
22 50, 111-136.
- 23 Liégeois, J.P., Benhallou, A., Azzouni-Sekkal, A., Yahiaoui, R., Bonin, B., 2005. The Hoggar
24 swell and volcanism: reactivation of the precambrian Tuareg shield during alpine
25 convergence and West African Cenozoic volcanism. In: Foulger, G.R., Natland, J.H.,
26 Presnall, D.C., Anderson, D.L. (Eds.), Plates, Plumes and Paradigms. *Geological Society of
27 America, Special Papers*, 388, 379-400.
- 28 Lompo, M., 2010. Structural evolution of Paleoproterozoic belts (Eburnean event) in the Man-
29 Leo Shield, West African Craton. Key structures for vertical to transcurrent tectonics.
30 *Journal of African Earth Sciences*, 58, 19-36.
- 31 Lüdtke, G., Hirdes, W., Konan, G., Koné, Y., Yao, C., Zamblé, Z., 1998. Géologie de la région
32 Haute Comoé Nord. *Ministère des ressources minières et pétrolières de Côte d'Ivoire*,
33 *Direction de la Géologie Abidjan*, 178p.

- 1 Lüdtke, G., Hirdes, W., Konan, G., Koné, Y., Yao, C., Diarra, S., Zamblé, Z., 1999. Géologie
2 de la région Haute Comoé Nord avec carte géologique 1/100,000. Feuilles Kong (4b et 4d)
3 et Téhini-Bouna (3a-3d). *République du Côte d'Ivoire Union Discipline Travail, Ministère*
4 *des Ressources Minières et Pétrolières, Direction de la Géologie* (Ed.), XV, 178p.
- 5 Luo, Y., Xue, D.-J., Wang, M., 2010. Reduction to the pole at the geomagnetic equator. *Chinese*
6 *Journal of Geophysics*, 53(6), 1082-1089.
- 7 MacLeod, I.C., Jones, K., Fan Dai, T., 1993. 3-D analytic signal in the interpretation of total
8 magnetic field data at low magnetic latitudes. *Exploration Geophysics*, 24, 679-688.
- 9 Markwitz, V., Hein, K.A.A., Jessell, M.W., Miller, J., 2016. Metallogenic portfolio of the West
10 Africa craton. *Ore Geology Reviews*, 78, 558-563.
- 11 Masurel, Q., Thébaud, N., Miller, J., Ulrich, S., 2017. The tectono-magmatic framework to gold
12 mineralisation in the Sadiola-Yatela gold camp and implications for the paleotectonic setting
13 of the Kédougou-Kéniéba inlier, West Africa. *Precambrian Research*, 292, 35-56.
- 14 McFarlane, H.B., Ailleres, L., Betts, P., Ganne, J., Baratoux, L., Jessell, M.W., Block, S., 2019.
15 Episodic collisional orogenesis and lower crust exhumation during the Paleoproterozoic
16 Eburnean Orogeny: Evidence from the Sefwi Greenstone Belt, West African Craton.
17 *Precambrian Research*, 325, 88-110.
- 18 Metelka, V., Baratoux, L., Naba, S., Jessell, W.M., 2011. A geophysically constrained litho-
19 structural analysis of the Eburnean greenstone belts and associated granitoid domains,
20 western Burkina-Faso. *Precambrian Research*, 190, 48-69.
- 21 Mériaud, N., Masurel, Q., Thébaud, N., Tourigny, G., 2019. Fluid pressure dominated orogenic
22 gold mineralization under low differential stress: case of the Yaouré gold camp, Côte
23 d'Ivoire, West Africa. *Mineralium Deposita*, 1-18.
- 24 Milési, J.P., Diallo, M., Dommagnet, A., Feybesse, J.L., Keita, F., Ledru, P., Vinchon, C., 1986.
25 Caractérisation litho-structurale de deux ensembles successifs dans les séries Birrimiennes
26 de la Boutonnière de Kédougou (Mali-Sénégal) et du Niandan (Guinée); implications
27 géologiques. *Centre International pour la Formation et les Echanges Géologiques*, 10, 113-
28 121.
- 29 Milési, J.P., Feybesse, J.L., Ledru, P., Dommagnet, A., Ouedraogo, M.F., Marcoux, E., Prost,
30 A., Vinchon, C., Sylvain, J.P., Johan, V., Tegye, M., Calvez, J.Y., Lagny, P., 1989.
31 Minéralisations aurifères de l'Afrique de l'Ouest, leurs relations avec l'évolution litho-
32 structurale au Protérozoïque inférieur. Carte géologique au 1/2000000. *Chronique de la*
33 *Recherche Minière*, 497, 3-98.

- 1 Milligan, P.R., Gunn, P.J., 1997. Enhancement and presentation of airborne geophysical data.
2 AGSO, *Journal of Australian Geology & Geophysics*, 17(2), 63-75.
- 3 Murray, S., Torvela, T., Bills, H., 2019. A geostatistical approach to analyzing gold distribution
4 controlled by large-scale fault systems – An example from Côte d’Ivoire. *Journal of African*
5 *Earth Sciences*, 151, 351-370.
- 6 Nabighian, M.N., 1974. Additional comments on the analytic signal of two-dimensional
7 magnetic bodies with polygonal cross-section. *Geophysics*, 39(1), 85–92.
- 8 Nomade, S., Chen, Y., Pouclet, A., Féraud, G., Théveniaut, H., Daouda, B.Y., Vidal, M.,
9 Rigolet, C., 2003. The Guiana and the West African Shield Palaeoproterozoic grouping: new
10 palaeomagnetic data for French Guiana and the Ivory Coast. *Geophysical Journal*
11 *International*, 154, 677-694.
- 12 Nunoo, S., Manu, J., Olarewaju, V.O., Asiedu, D.K., Nude, P.M., 2016. Deciphering structures
13 and deformation of the Obuom Gold Prospect, Central Ashanti Belt of Ghana: A
14 lithostructural approach. *Journal of African Earth Sciences*, 124, 159-170.
- 15 Nunoo, S., Hofmann, A., Kramers, J., 2022. Geology, zircon U–Pb dating and ϵ Hf data for the
16 Julie greenstone belt and associated rocks in NW Ghana: Implications for Birimian-to-
17 Tarkwaian correlation and crustal evolution. *Journal of African Earth Sciences*, 186,
18 104444.
- 19 Okubo, Y., Graf, R.J., Hansen, R.O., Ogawa, K., Tsu, H., 1985. Curie point depths of the island
20 of Kyushu and surrounding areas, Japan. *Geophysics*, 50, 481-494.
- 21 Osinowo, O.O., Alumona, K., Olayinka, A.I., 2020. Analyses of high resolution aeromagnetic
22 data for structural and porphyry mineral deposit mapping of the Nigerian younger granite
23 ring complexes, North-Central Nigeria. *Journal of African Earth Sciences*, 162, 103705.
- 24 Perrouy, S., Ailleres, L., Jessell, M.W., Baratoux, L., Bourassa, Y., Crawford, B., 2012.
25 Revised Eburnean geodynamic evolution of the gold-rich southern Ashanti belt, Ghana, with
26 new field and geophysical evidence of pre-Tarkwaian deformations. *Precambrian Research*,
27 204-205, 12-39.
- 28 Peschler, A.P., Benn, K., Roest, W.R., 2004. Insights on Archean continental geodynamics
29 from gravity modelling of granite-greenstone terranes. *Journal of Geodynamics*, 38, 185-
30 207.
- 31 Peschler, A.P., Benn, K., Roest, W.R., 2006. Gold-bearing fault zones related to Late Archean
32 orogenic folding of upper and middle crust in the Abitibi granite greenstone belt, Ontario.
33 *Precambrian Research*, 151, 143-159.

1 Piazzolo, S., Passchier, C.W., 2002. Controls on lineation development in low to medium grade
2 shear zones: a study from the Cap de Creus peninsula, NE Spain. *Journal of Structural*
3 *Geology*, 24, 25-44.

4 Pouclet, A., Doumbia, S., Vidal, M., 2006. Geodynamic setting of the Birimian volcanism in
5 Central Cote d'Ivoire (western Africa) and its place in the Palaeoproterozoic evolution of the
6 man shield. *Bulletin de la Société Géologique de France*, 177, 105-121.

7 Reid, A.B., Allsop, J.M., Granser, H., Millett, A.T., Somerton, I.W., 1990. Magnetic
8 interpretation in three dimensions using Euler deconvolution. *Geophysics*, 55(1), 80-91.

9 Roest, W.R., Verhoef, J., Pilkington, M., 1992. Magnetic interpretation using the 3-D analytic
10 signal. *Geophysics*, 57, 116-125.

11 Salem, A., Williams, S., Fairhead, J.D., Ravat, D., Smith, R., 2007. Tilt-depth method - a simple
12 depth estimation method using first-order magnetic derivatives. *The Leading Edge*, 26,
13 1502-1505.

14 Salem, A., Williams, S., Samson, E., Fairhead, D., Ravat, D., Blakely, R.J., 2010. Sedimentary
15 basins reconnaissance using the magnetic tilt-depth method. *Exploration Geophysics*, 41,
16 198-209.

17 Santos, L.C.M.L., Dantas, E.L., Vidotti, R.M., Cawood, P.A., Santos, E.J., Fuck, R.A., Lima,
18 H.M., 2017. Two-stage terrane assembly in Western Gondwana: Insights from structural
19 geology and geophysical data of central Borborema Province, NE Brazil. *Journal of*
20 *Structural Geology*, 103, 167-184.

21 Siagné, Z.H., Aïfa, T., Kouamelan, A.N., Houssou, N.N., Digbeu, W., 2021. Analyse
22 structurale de la déformation dans les granitoïdes éburnéens de la Région de Doropo (Nord-
23 Est de la Cote d'Ivoire). *European Scientific Journal*, 17, 157-172.

24 Spector, A., Grant, F.S., 1970. Statistical models for interpreting aeromagnetic data.
25 *Geophysics*, 35, 293-302.

26 Stewart, J.R., Betts, P.G., 2010. Late Paleo-Mesoproterozoic plate margin deformation in the
27 southern Gawler Craton: Insights from structural and aeromagnetic analysis. *Precambrian*
28 *Research*, 177, 55-72.

29 Tagini, B., 1971. Esquisse structurale de la Côte d'Ivoire. Essai de géotectonique régionale.
30 *Thèse de doctorat ès sciences*, Fac. Sci., Univ. Lausanne, *Rapport SODEMI*, Abidjan, 266p.

31 Tanaka, A., Okubo, Y., Matsubayashi, O., 1999. Curie point depth based on spectrum analysis
32 of the magnetic anomaly data in East and Southeast Asia. *Tectonophysics*, 306, 461-470.

- 1 Teha, K.R., 2019. Les formations éburnéennes du Sud-Ouest du bassin de la Comoé et du
2 secteur de Singrobo (Sud de la Côte d'Ivoire) : pétrologie, analyse structurale et magmatisme
3 associé. *Thèse de doctorat, Université Felix Houphouët-Boigny (Côte d'Ivoire)*, 247p.
- 4 Thiéblemont, D., 2005. Géologie et pétrologie de l'Archéen de Guinée: une contribution
5 régionale à la formation de la croûte continentale. *Unpublished PhD thesis*, University of
6 Brest, France, 149p.
- 7 Thompson, D.T., 1982. EULDPH: A new technique for making computer-assisted depth
8 estimates from magnetic data. *Geophysics*, 47, 31-37.
- 9 Tourigny, G., Tranos, M.D., Masurel, Q., Kreuzer, O., Brammer, S., Owusu-Ansah, K., Yao,
10 D., Hayford, T., 2019. Structural controls on granitoid-hosted gold mineralization and
11 paleostress history of the Edikan gold deposits, Kumasi Basin, southwestern
12 Ghana. *Mineralium Deposita*, 54, 1033-1052.
- 13 Tshibubudze, A., Hein, K.K.A, Peters, L.F.H., Woolfe, A.J., McCuaig, T.C., 2013. Oldest U-
14 Pb crystallization age for the West African Craton from the Oudalan-Gorouol Belt of
15 Burkina-Faso. *South African Journal of Geology*, 116, 169-181.
- 16 Vanderhaege, O., Ledru, P., Thiéblemont, D., Egal, E., Cocherie, A., Tegye, M., Milesi, J.,
17 1998. Contrasting mechanism of crustal growth geodynamic evolution of the
18 Paleoproterozoic granite-greenstone belts of French Guiana. *Precambrian Research*, 92,
19 165-193.
- 20 Vidal, M., Delor, C., Pouclet, A., Simeon, Y., Alric, G., 1996. Evolution géodynamique de
21 l'Afrique de l'Ouest entre 2.2 Ga et 2 Ga: Le style archéen des ceintures vertes et des
22 ensembles sédimentaires birimiens du nord-est de la Côte d'Ivoire. *Bulletin de la Société
23 Géologique de France*, 167, 307-319.
- 24 Vidal, M., Gumiaux, C., Cagnard, F., Pouclet, A., Ouattara, G., Pichon, M., 2009. Evolution of
25 a Paleoproterozoic "weak type" orogeny in the West African Craton (Ivory Coast).
26 *Tectonophysics*, 477, 145-159.

27

28 **Table captions**

29 **Table 1:** Synthesis of tectonic evolution highlighted during the different studies in the southern
30 part of WAC (modified after [Baratoux et al., 2011](#)).

31 **Table 2:** Structural indexes of Euler deconvolution solutions according to geological models
32 responsible for magnetic anomalies ([Reid et al., 1990](#)). SI: structural index, DS: depth to the
33 surface, DC: depth to the centroid.

1 **Table 3:** Magnetic susceptibility values measured in the field (see Fig. 4) and in the laboratory
2 (see Fig. 5) and their statistical processing ($10^{-3}SI$). N, Min, Max, Mean, St err, var, St Dev,
3 Median, Geom Mean: number of samples, minimum, maximum and mean values, standard
4 error, variance, standard deviation, median and geometric mean, respectively.
5

6 **Figure captions**

7 **Fig. 1:** Schematic geological map of the West African Craton. The inset shows the location
8 map of the WAC (red square).

9 **Fig. 2:** (a) Geological map of the study area (modified from Tagini, 1971; Murray et al., 2019).
10 Numbers represent shots of Figs. 6-9. (b) Details of the outcrop area with the sampling sites
11 (stars).

12 **Fig. 3:** Field photographs of the main lithologies from the Doropo region. (a) Biotite granite,
13 (b) Gneissic granite crossed by pegmatitic vein, (c) Migmatitic granite with mafic enclaves,
14 (d) Outcrop of granodiorite, (e) Gabbro crossed by quartzofeldspathic vein, (f) Amphibolite
15 with numerous thin quartz and feldspar veins, (g) Rhyolite boulders, and (h) Dolerite dyke in
16 drill core.

17 **Fig. 4:** Histogram of the magnetic susceptibility values of the different lithologies measured in
18 the field (in situ) on the following facies: (a) Biotite granite, (b) Gneissic granite, (c)
19 Granodiorite, (d) Gabbro and (e) Amphibolite, with their Gaussian and density distributions.

20 **Fig. 5:** Histogram of the magnetic susceptibility values of the different lithologies measured in
21 the laboratory on samples taken from the following facies: (a) Biotite granite, (b) Gneissic
22 granite, (c) Granodiorite, (d) Gabbro, (e) Amphibolite, (f) Rhyolite, (g) Dolerite, with their
23 Gaussian and density distributions and (h) normalized histogram of all these facies.

24 **Fig. 6:** Structures of the D_1 deformation observed in the field. (a) E-W Foliation (S_1) in the
25 gneissic granite of Doropo; (b) F_1 Fold in the gneissic granite of Bouko; (c) NE-SW sinistral
26 shear in the migmatitic granite of Lagbo; (d) NW-SE dextral shear in the gneissic granite of
27 Doropo and (e) Directional rose diagram of major structures in the field. The tip of the
28 compass indicates the North direction on the different field photos.

29 **Fig. 7:** Representative structures of the D_2 deformation. (a) NE-SW Foliation (S_2) within the
30 gneissic granite of Bouko; (b) Stretching L_2 lineation within Bouko's gneissic granite; (c) E-
31 W dextral shear observed at Bouko and (d) S-C fabrics in the Lagbo's migmatitic granite; (e)
32 Directional rose diagram of the major structures in the field.

33 **Fig. 8:** Structures of the D_3 deformation. (a) NW-SE Foliation (S_3) in the migmatitic granite of
34 Lagbo; (b) WNW-ESE sinistral shear in Lagbo migmatitic granite; (c) F_3 Fold with an NW-

1 SE axial plane observed at Gbatedjou and **(d)** directional rose diagram of the S_3 foliation. P
2 denotes the axial plane of the fold.

3 **Fig. 9:** Structures of the D_4 deformation. **(a)** Microgranite dyke dextrally shearing a pegmatite
4 dyke; **(b)** Conjugated fractures within the Gbatedjou microgranite; **(c)** Fault mirror with
5 subhorizontal slickenslide lineations reflecting a sinistral shear; **(d)** Fracture plan showing an
6 infill with epidote or chlorite. Directional rose diagrams for the analyzed structures are also
7 given.

8 **Fig. 10:** **(a)** Map of the total magnetic field using shaded relief technique ($I = 45^\circ$ and $D = 45^\circ$);
9 **(b)** Map of the magnetic field reduced to pole. Ap_1 - Ap_3 and An_1 - An_3 are positive and negative
10 magnetic anomalies, respectively.

11 **Fig. 11:** Upward continuation maps at **(a)** 100 m, **(b)** 200 m, **(c)** 500 m and **(d)** 1000 m. Same
12 notations as in [Fig. 10](#).

13 **Fig. 12:** Gradient maps according to **(a)** X; **(b)** Y; **(c)** Z and **(d)** Structural sketch related to
14 faults, shears, dykes and magnetic lineaments superimposed on the derivative map according
15 to Y.

16 **Fig. 13:** Analytical signal map showing geological bodies of the same nature. Areas within the
17 white dotted lines show NW-SE and NE-SW oriented structures.

18 **Fig. 14:** Map of the Tilt Derivative showing linear (faults, shears) and massive structures with
19 curvilinear magnetic lineaments (white lines).

20 **Fig. 15:** Power spectral diagram ([Spector and Grant, 1970](#)) showing three possible depths of
21 the causative sources at 55 m, 125 m and 425 m.

22 **Fig. 16:** Map of the 3D Euler deconvolution solutions for depth plans in the ranges **(a)** 50-75
23 m: shows NE-SW and NW-SE oriented linear structures; **(b)** 75-100 m: highlights the same
24 linear structures as in **(a)**; **(c)** 150-200 m: the linear structures tend to disappear except some
25 NE-SW structures (e.g., northwestern the map) and **(d)** 300-400 m: all linear structures
26 disappeared.

27 **Fig. 17:** Lithostructural map of the Doropo region (reduction of the 1:50,000 scale map).

28 **Fig. 18:** Tectonic model proposed for the Doropo region during the Eburnean. **(a)** crustal
29 thickening and emplacement of granitoids, **(b)** occurrence of oblique shears, **(c)** reactivation
30 of faults and magmatic inflows. Red arrow indicates the σ_1 direction.

31
32
33
34

1

2 **Highlights**

3

4 • Four deformation phases (D₁-D₄) recognized in northeast of Côte d'Ivoire.

5 • Evidence of NE-SW and NW-SE dolerite dykes and shear zones from aeromagnetic maps.

6 • Causative magnetic sources at 55 m, 125 m and 425 m depths identified using spectral analysis
7 and 3D Euler deconvolution solutions.

8 • New lithostructural map of the Doropo region at a scale of 1:50,000 derived from field
9 observations and aeromagnetic data processing.

10 • Proposition of a geodynamic model evolution for the Doropo region.

Table 1

Authors	Location	Tectonic evolution
Milési et al. (1989)	Man-Leo shield	Birimian flysch sediment deposition followed by volcanism
		D ₁ : Tectonic Nappe, ENE-suture between Archean and Proterozoic terranes (Burkinian cycle)
		D ₂ : N-E folds, N to N-E shear zones (Birimian cycle), transpression
Vidal et al. (1996)	N-E Côte d'Ivoire	D ₃ : N-E shear zones and crenulation cleavage
		Ante-Birimian (Dabakalian) deposition
		D ₁ : Metamorphic fabric, gently dipping crenulation cleavage (Dabakalian)
		D ₂ : N-E folds
Lüdke et al. (1998)	N-E Côte d'Ivoire	D ₃ : N-S sinistral and WNW shear zones, transpression
		D ₄ : WNW crenulation cleavage, S-thrusting
		D ₀ : Volcanism and deposition sediment Birimian
		D ₁ : Juxtaposition of low and high grade metamorphic, NNE steep shear zones
Feybesse et al. (2006)	Ghana	D ₂ : N-E folds, NNE sinistral shear zones, metamorphic fabric
		D ₃ : NE-SW shear zones and E-shear zones, crenulation cleavage
		D ₄ : Reactivation of existing structures, N-E dolerite dykes
Hein (2010)	Goren greenstone belt (Burkina-Faso)	Volcano-plutonism, Birimian flysch sediment deposition
		D ₁ : Crustal thickening by nappe stacking, shearing to the N-W
		D ₂ -D ₃ : N-E sinistral shear zones, WNW shortening brittle shearing. Steep folds, crenulation cleavage
Baratoux et al. (2011)	Western Burkina-Faso	Volcanism and deposition sediment (Birimian)
		D ₁ : N-W to NNW folds, thrust faults (Tangaen)
		D ₂ : NNE to N-E sinistral shear zones, metamorphic fabric, crenulation cleavage
		D ₃ : WNW dextral thrust faults, E-W folds. Following by mafic dykes (250 Ma)
Baratoux et al. (2011)	Western Burkina-Faso	Early Eburnean extensional deformation: ca. 2200-2160 Ma, volcanic arc, Birimian sediment deposition
		Early Eburnean ca. 2170-2160 Ma
		D ₁ : ca. 2160-2120 Ma, N-E metamorphic fabrics, shear zones, isoclinal folds WNW-ESE compression
Baratoux et al. (2011)	Western Burkina-Faso	Late D ₁ : ca. 2120-2110 Ma, detrital sedimentary deposition (Tarkwaian), E-W transtension
		D ₂ : ca. 2110-2109 Ma, N-S to ENE steep shear zones, N-W faults, NW-SE transpression

		<p>D₃: Post-2109 Ma, E-W crenulation cleavage, N-W-faults, thrusts, N-S compression</p> <p>Mafic dykes: post-2109 Ma, NE-SW, NW-SE and WNW-ESE extension</p>
		<p>Sefwi group volcanism and sedimentation</p> <p>D₁: N-S shortening, regional scale folding in the Sefwi group, possible gold mineralization</p> <p>D₂: Extension phase (2154-2125 Ma), Kumasi group sedimentation</p> <p>Tarkwa Basin formation (2107-2097 Ma) / D₃: Km scale folds in Birimian and Tarkwaian, NE-SW subvertical crenulation cleavage, thrust faults (Ashanti, Damang, ...), peak of metamorphism (2092 Ma)</p> <p>D₄: NNW-SSE shortening, sinistral shear reactivation of D₃ thrust, ENE-WSW crenulation cleavage, greenschist retrograde metamorphism, remobilization and concentration of gold particle along the shear zones and at the base of Tarkwa Basin</p> <p>D₅: Recumbent folds (< m), subhorizontal crenulation cleavage, last pyrite/gold mineralization associated with quartz vein</p> <p>D₆: Shortening NE-SW, low amplitude folds + crenulation cleavage ~N320°/70° (RH), reverse faults oriented NW-SE</p>
		<p>Relics of early deformation</p> <p>D₁: N-S shortening, penetrative fabric associated with shear zones and large-scale folds</p> <p>D₂: N-S extension, moderate foliation dip (40-50°), stretching lineation plunging down-dip</p> <p>D₃: E-W shortening, subvertical schistose cleavage, axial planar to isoclinal or ptygmatic folds, high-strain shear bands</p> <p>D₄: ENE-WSW shortening and localized sinistral strike-slip shearing, activation of the Jirapa and Jan shear zones under a dominant sinistral strike-slip regime, subhorizontal lineation</p> <p>D₅: E-W shortening and localized dextral strike-slip shearing, subvertical dextral strike-slip shear zones</p> <p>D₆: E-W shortening, brittle deformation, E-W quartz tension gashes, conjugate brittle strike-slip faults</p> <p>D₇: NE-SW shortening, brittle deformation, NW-SE subvertical crenulation cleavage</p>
		<p>D₁: NNW-SSE Shortening, isoclinal folding, thrusting, high-grade metamorphism, and late-stage partial melting</p> <p>D₂: ENE-WSW transtension, tight to open folds, stretching lineation, S-C fabrics, NE-subvertical foliation</p> <p>D₃: E-W shortening, N-S-subvertical crenulation cleavage, axial planar to open gently north-plunging folds, sinistral drag folds, NE-SW S-C fabric</p> <p>D₄: NW-SE shortening, brittle ductile deformation and NNE-SSW sinistral shear zones</p> <p>D₅: WNW-ESE shortening, Riedel shear zones, late NW-SE, NE-SW and E-W structures which form conjugate faults</p>
Perrouty et al. (2012)	Southern Ashanti Belt (Ghana)	
Block et al. (2016)	N-W Ghana	
McFarlane et al. (2019)	Sefwi Greenstone Belt (Ghana)	

Table 2

Geological model	SI	Depth type
Deep depth contact or high fault offset	0	DS
Contact/limit/fault	0.5	DS
Layer limit (dyke, oblique intrusion, BIF, etc.)	1	DS
Linear sources (pipe, narrow kimberlitic chimney, etc.)	2	DC
Sphere or compact body	3	DC

Table 3

Facies	N	Min	Max	Mean	St err	Var	St Dev	Median	Geom Mean
Amphibolite	30	0.01	0.35	0.1286667	0.01775784	0.00946023	0.09726371	0.1	0.08844865
Dolerite	12	0.009	26.1	11.99658	2.458064	72.50497	8.514985	10.045	6.010357
Gabbro	30	0.03	0.23	0.1116667	0.01020574	0.003124713	0.05589913	0.11	0.09744356
Biotite Granite	222	0.01	12.2	1.593964	0.1099113	2.681867	1.637641	1.175	0.7078828
Gneissic Granite	30	0.55	9.98	3.683667	0.5145313	7.942272	2.818204	2.655	2.673775
Granodiorite	48	0.07	4.33	1.173542	0.1526702	1.118794	1.05773	0.96	0.663975
Rhyolite	30	0.009	1.5	0.1800333	0.06720845	0.1355093	0.3681158	0.02	0.0389743
Amphibolite	7	0.003	0.97	0.2991429	0.121254	0.1029178	0.3208081	0.184	0.1389352
Gabbro	8	0.22	0.36	0.289375	0.01677151	0.002250268	0.04743699	0.293	0.2858414
Biotite Granite	114	0.025	17.1	4.02286	0.3115148	11.06273	3.326068	3.985	0
Gneissic Granite	27	0.093	12.9	4.303963	0.602029	9.785851	3.128234	4.59	2.750815
Granodiorite	11	1.59	7.73	4.801818	0.5793803	3.692496	1.921587	4.42	4.403127

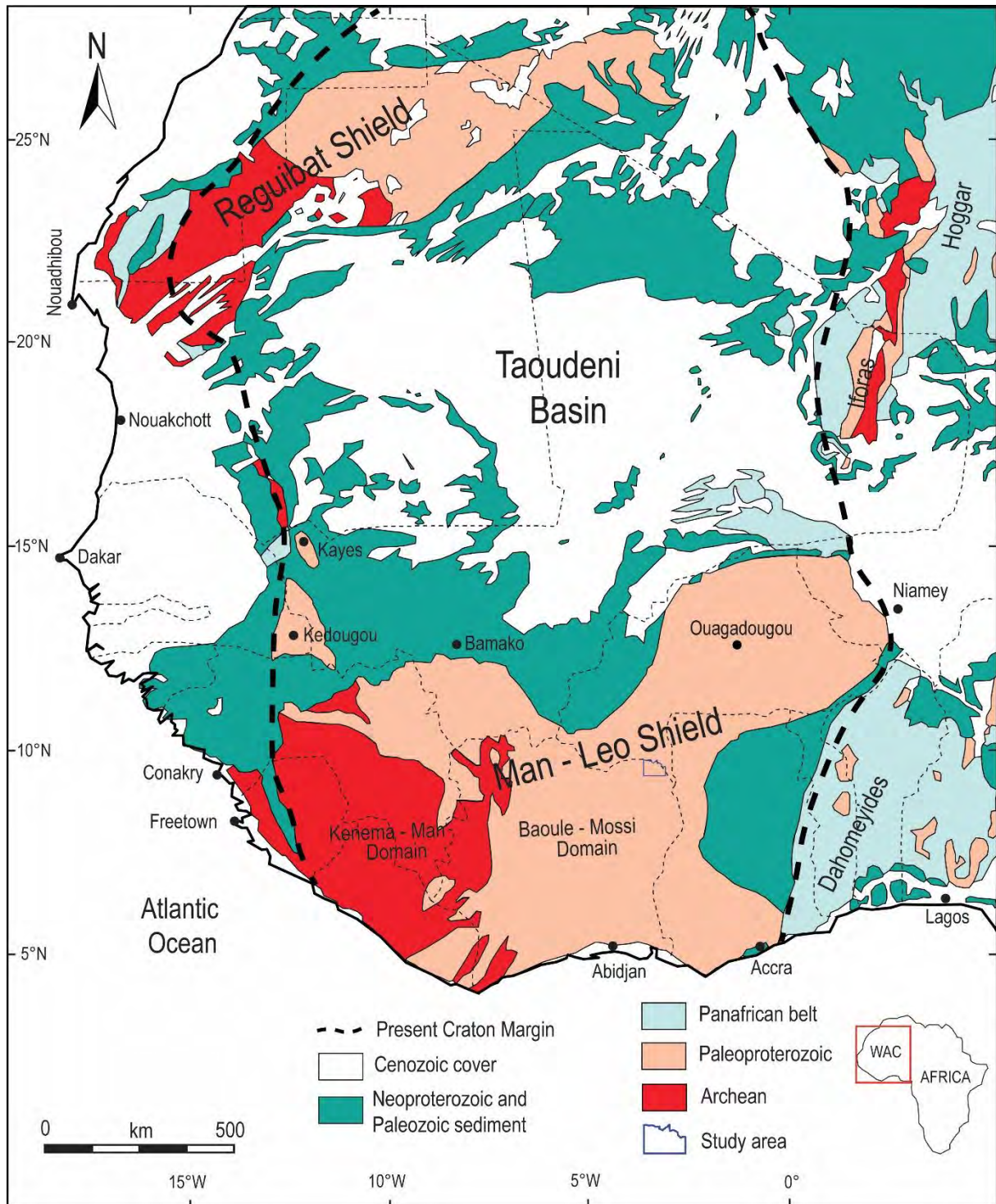


Fig. 1. Schematic geological map of the West African Craton. The inset shows the location map of the WAC (red square).

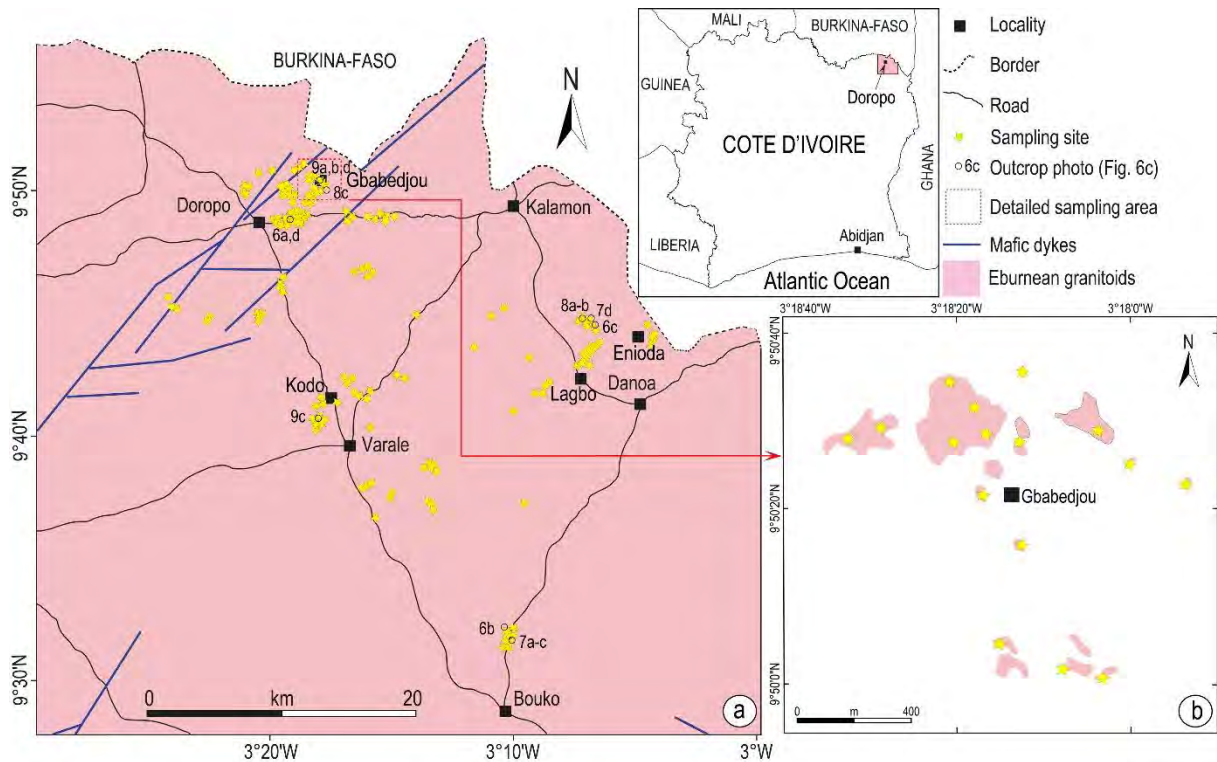


Fig. 2. (a) Geological map of the study area (modified from Tagini, 1971; Murray et al., 2019). Numbers represent shots of Figs. 6-9. (b) Details of the outcrop area with the sampling sites (stars).

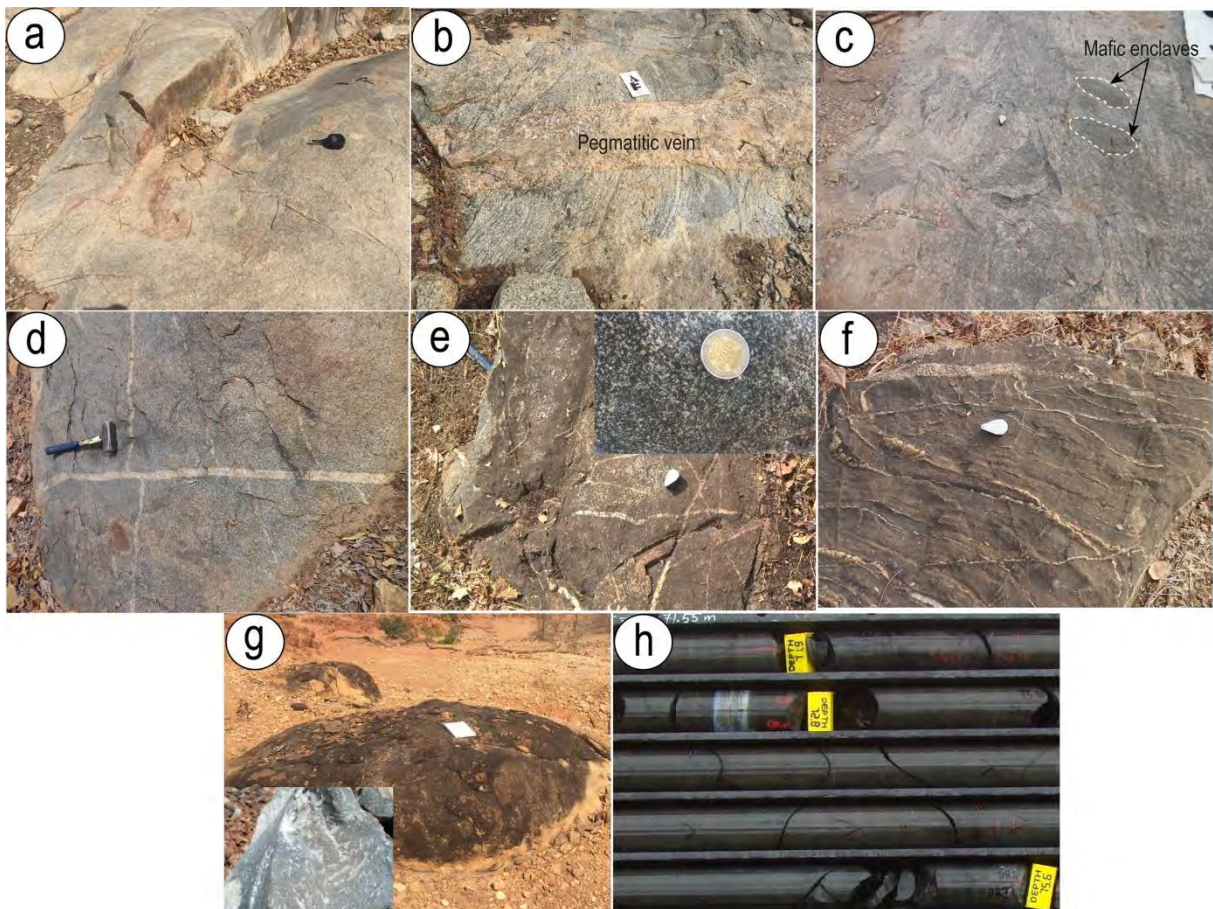


Fig. 3. Field photographs of the main lithologies from the Doropo region. (a) Biotite granite, (b) Gneissic granite crossed by pegmatitic vein, (c) Migmatitic granite with mafic enclaves, (d) Outcrop of granodiorite, (e) Gabbro crossed by

quartzofeldspathic vein, (f) Amphibolite with numerous thin quartz and feldspar veins, (g) Rhyolite boulders, and (h) Dolerite dyke in drill core.

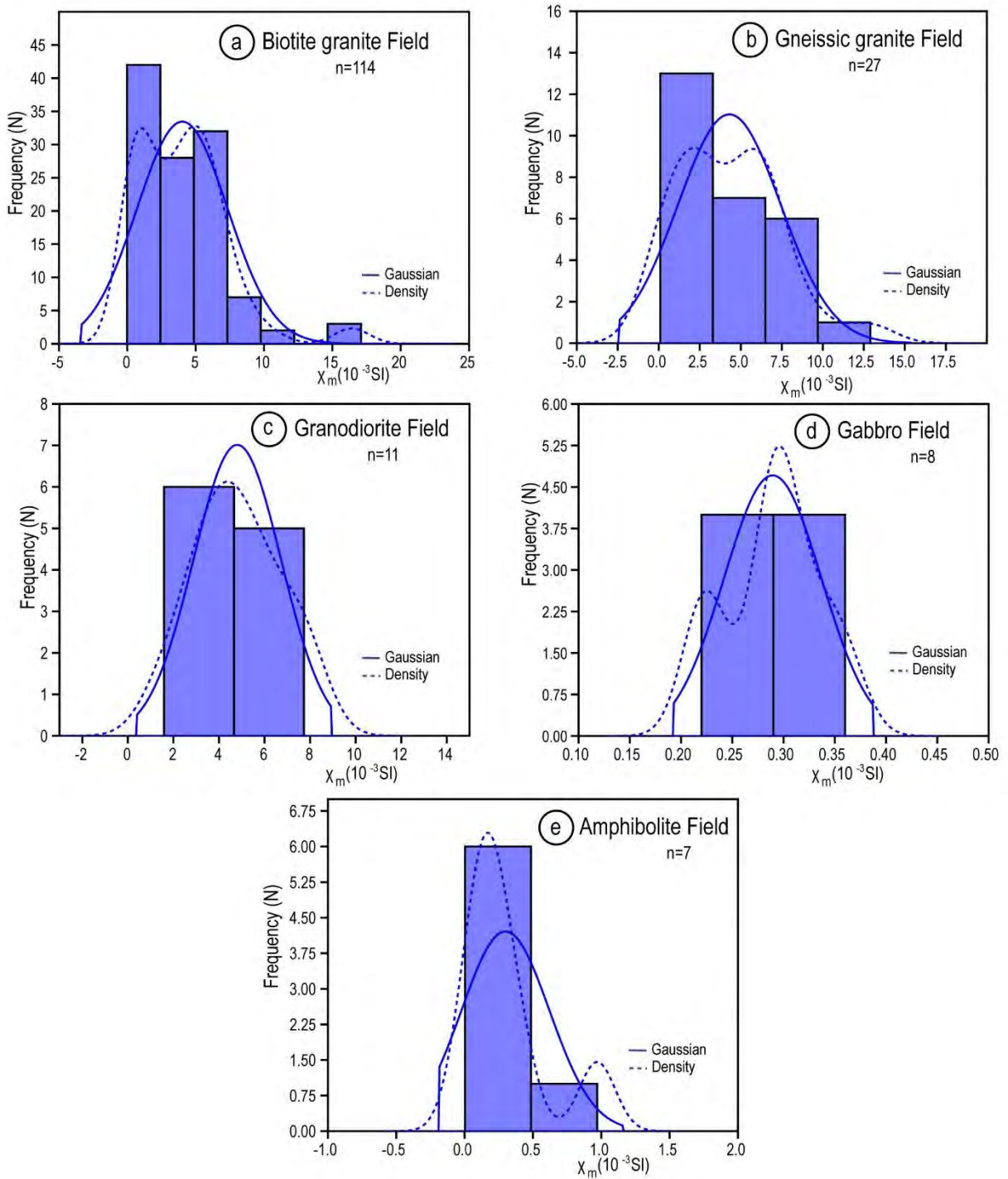


Fig. 4. Histogram of the magnetic susceptibility values of the different lithologies measured in the field (in situ) on the following facies: (a) Biotite granite, (b) Gneissic granite, (c) Granodiorite, (d) Gabbro and (e) Amphibolite, with their Gaussian and density distributions.

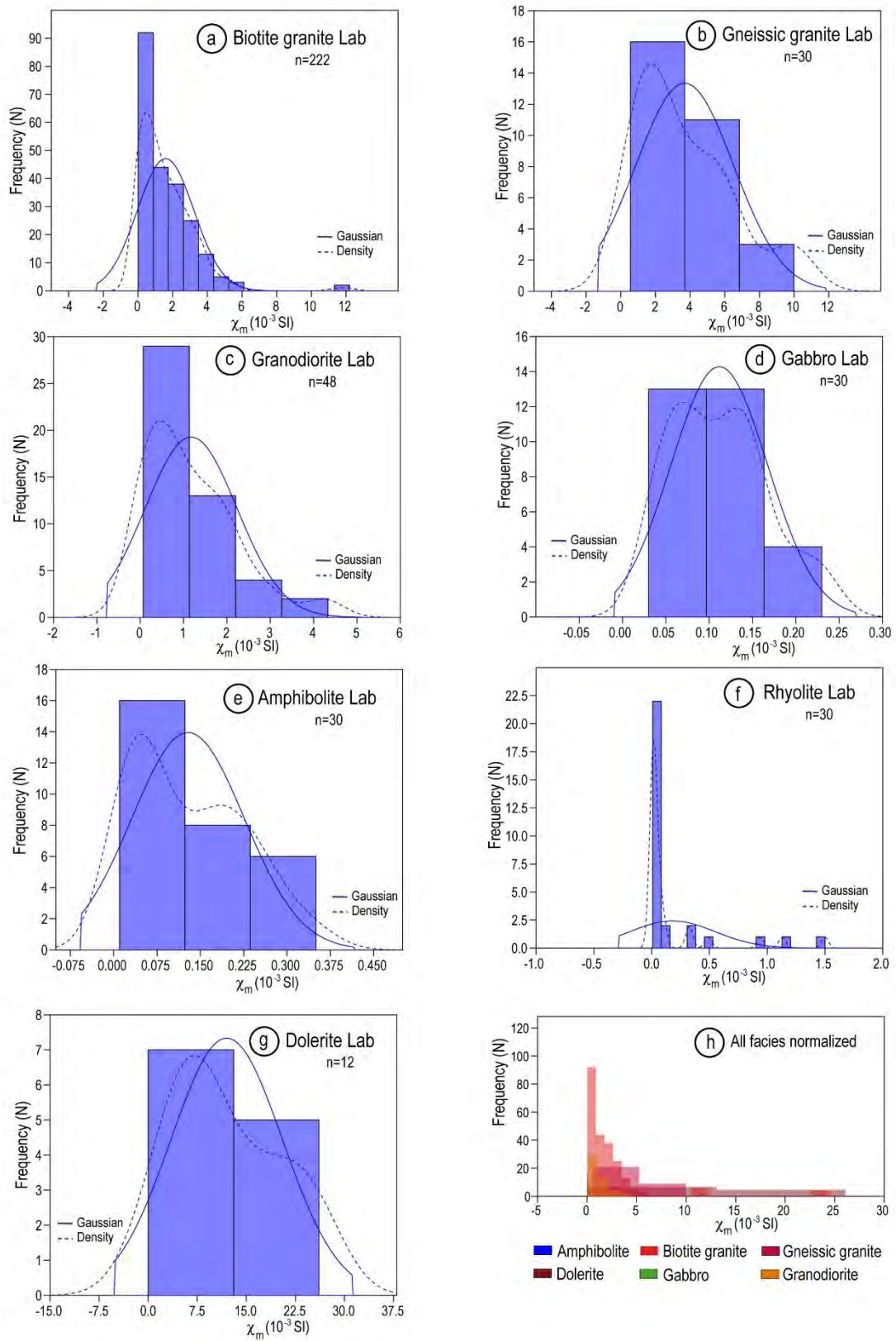


Fig. 5. Histogram of the magnetic susceptibility values of the different lithologies measured in the laboratory on samples taken from the following facies: (a) Biotite granite, (b) Gneissic granite, (c) Granodiorite, (d) Gabbro, (e) Amphibolite, (f) Rhyolite, (g) Dolerite, with their Gaussian and density distributions and (h) normalized histogram of all these facies.

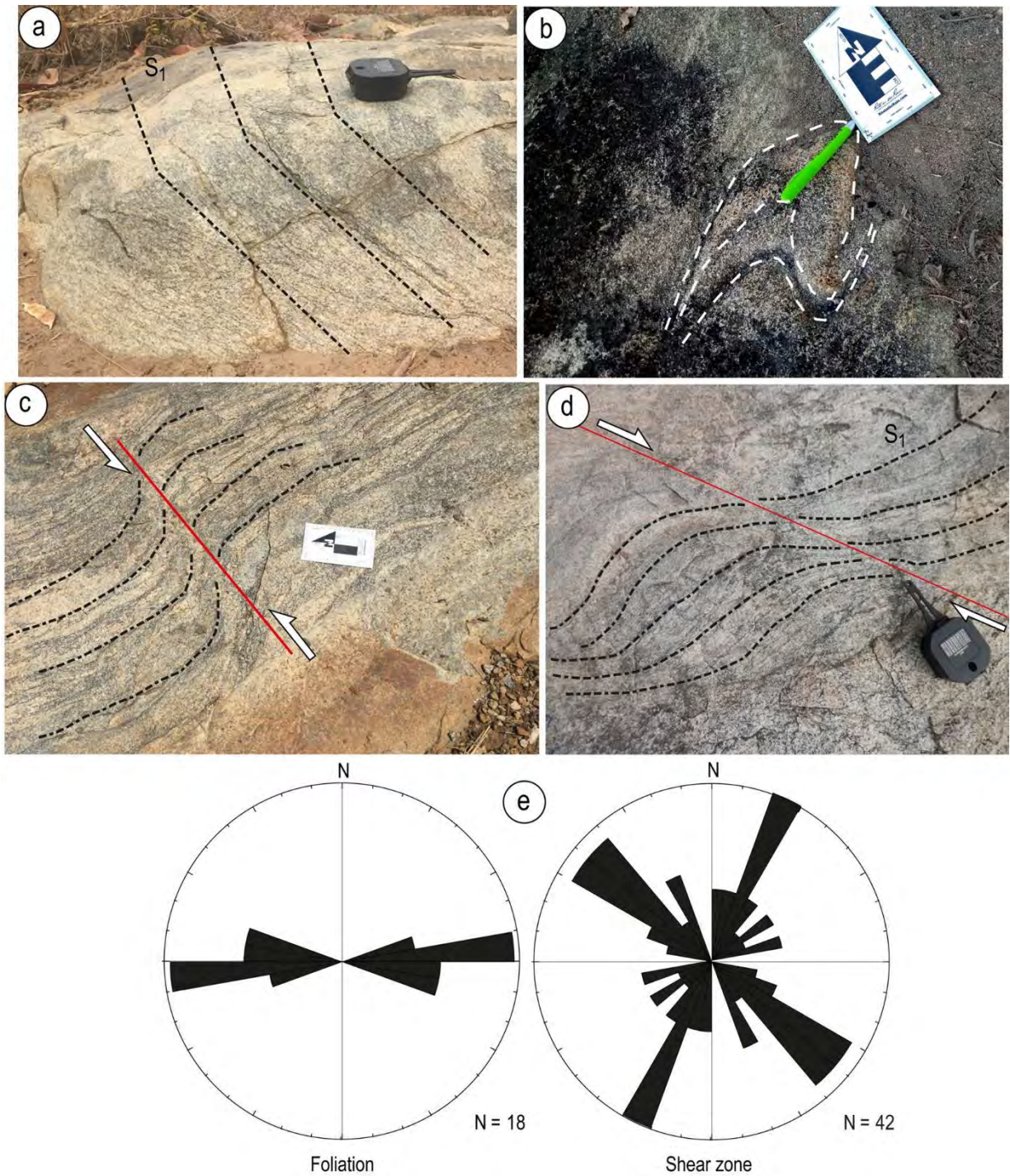


Fig. 6. Structures of the D₁ deformation observed in the field. (a) E-W Foliation (S₁) in the gneissic granite of Doropo; (b) F₁ Fold in the gneissic granite of Bouko; (c) NE-SW sinistral shear in the migmatitic granite of Lagbo; (d) NW-SE dextral shear in the gneissic granite of Doropo and (e) Directional rose diagram of major structures in the field. The tip of the compass indicates the North direction on the different field photos.

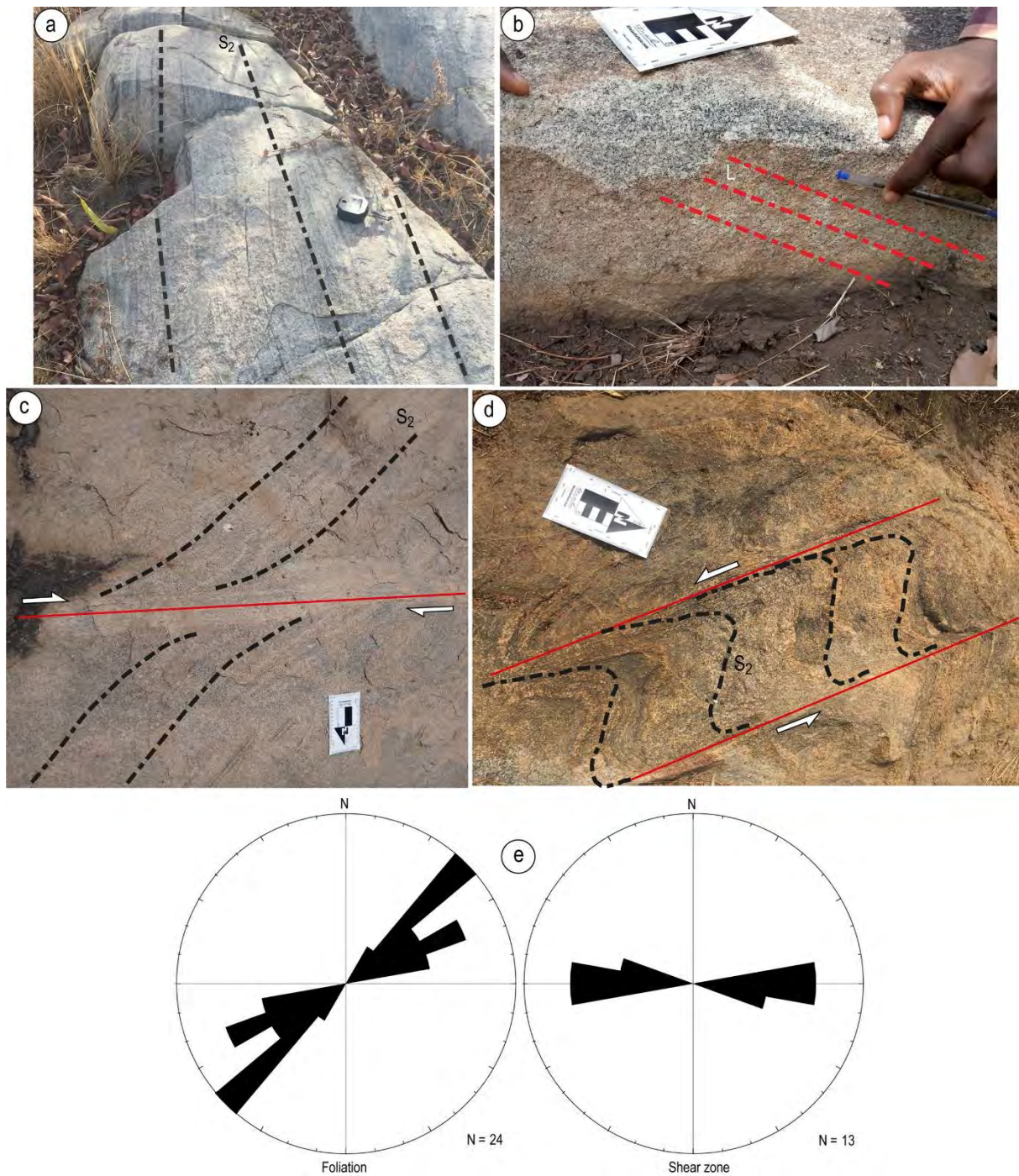


Fig. 7. Representative structures of the D_2 deformation. (a) NE-SW Foliation (S_2) within the gneissic granite of Bouko; (b) Stretching L_2 lineation within Bouko's gneissic granite; (c) E-W dextral shear observed at Bouko and (d) S-C fabrics in the Lagbo's migmatitic granite; (e) Directional rose diagram of the major structures in the field.

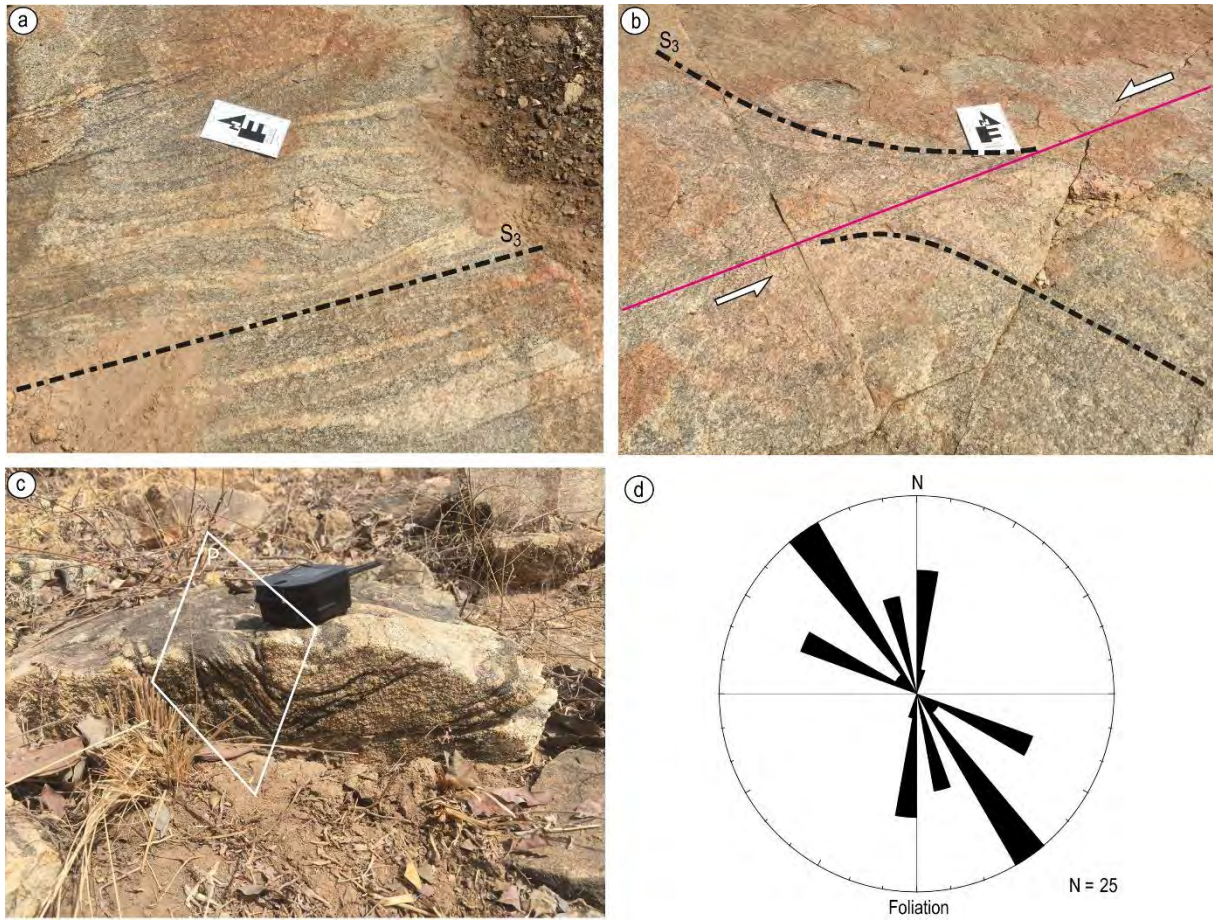


Fig. 8. Structures of the D_3 deformation. (a) NW-SE Foliation (S_3) in the migmatitic granite of Lagbo; (b) WNW-ESE sinistral shear in Lagbo migmatitic granite; (c) F_3 Fold with an NW-SE axial plane observed at Gbagedjou and (d) directional rose diagram of the S_3 foliation. P denotes the axial plane of the fold.

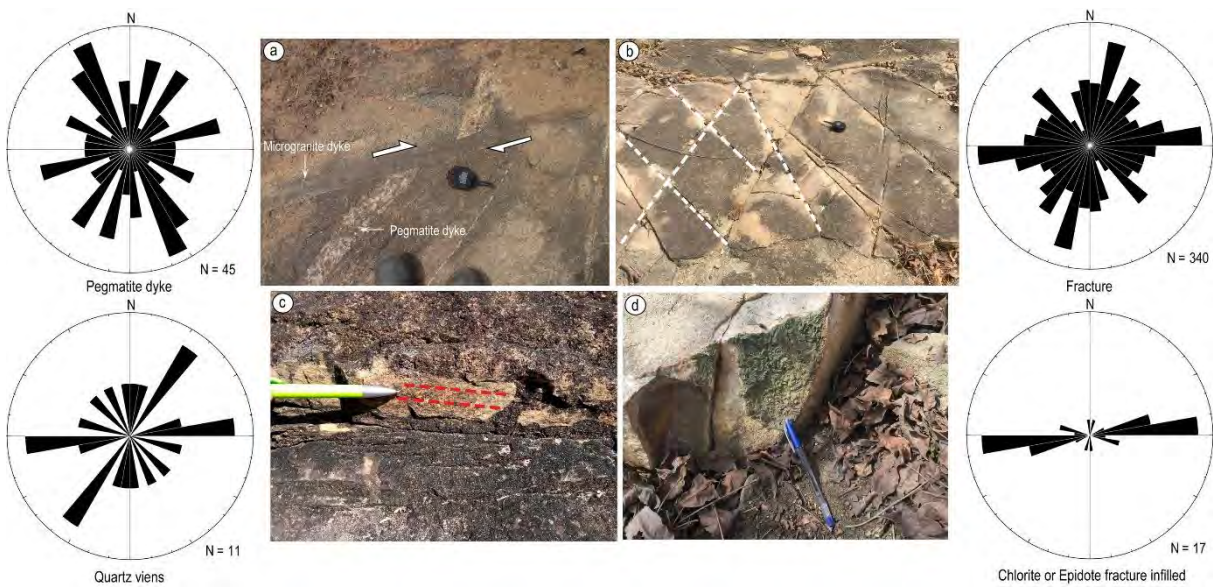


Fig. 9. Structures of the D_4 deformation. (a) Microgranite dyke dextrally shearing a pegmatite dyke; (b) Conjugated fractures within the Gbagedjou microgranite; (c) Fault mirror with subhorizontal slickenslide lineations reflecting a sinistral shear; (d) Fracture plan showing an infill with epidote or chlorite. Directional rose diagrams for the analyzed structures are also given.

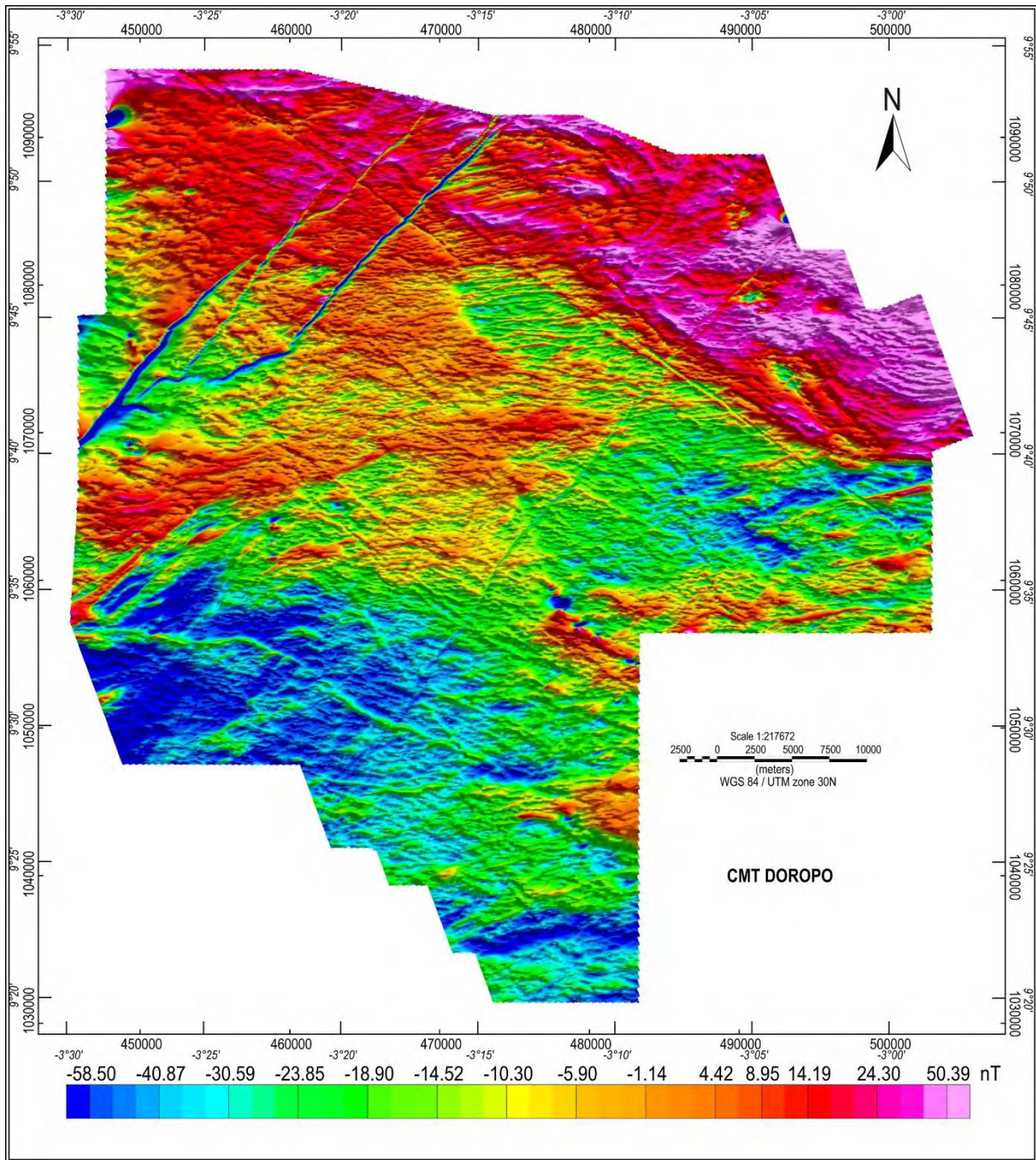


Fig. 10a. Map of the total magnetic field using shaded relief technique ($I = 45^\circ$ and $D = 45^\circ$).

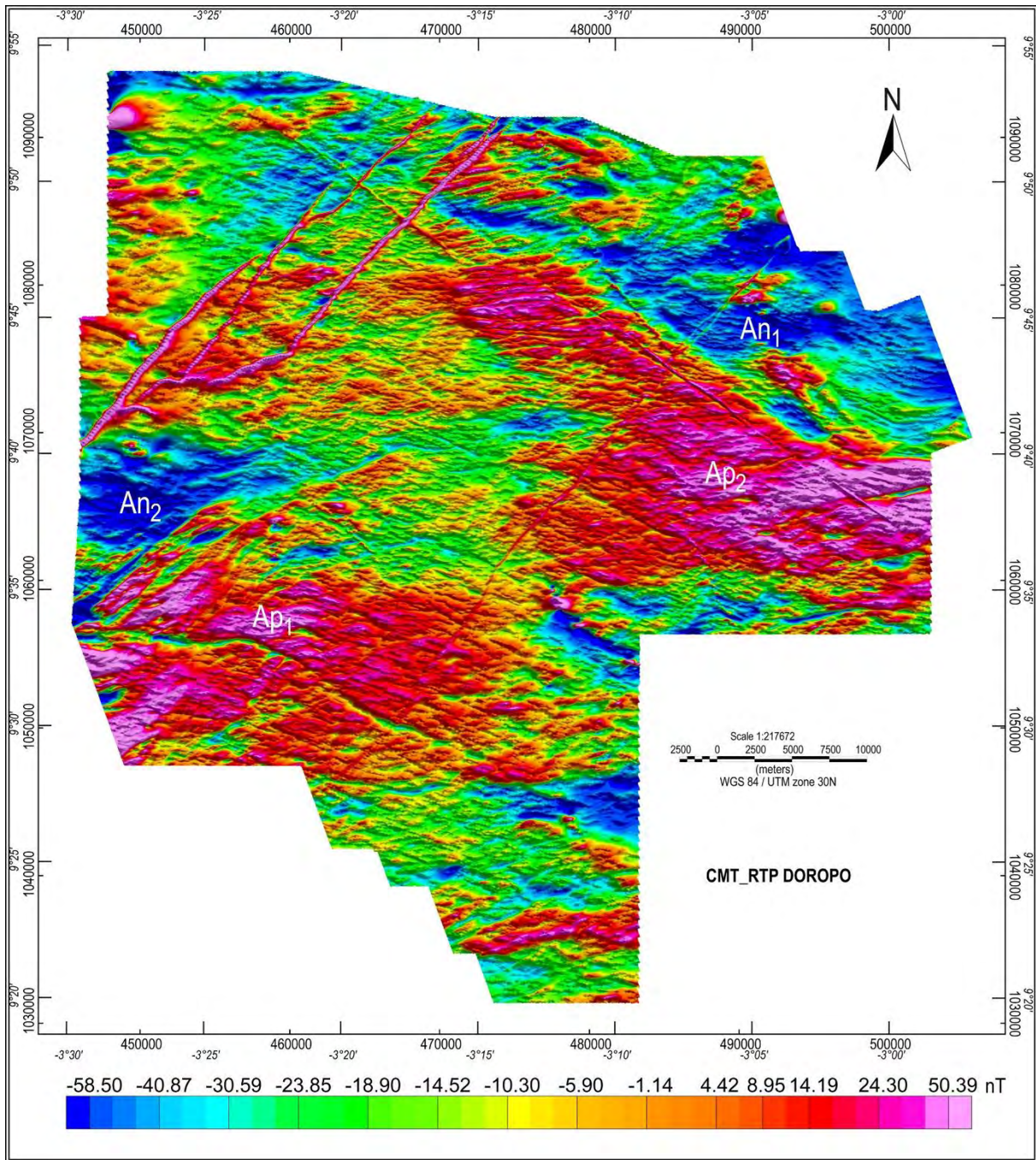


Fig. 10b. Map of the magnetic field reduced to pole. Ap₁- Ap₃ and An₁-An₃ are positive and negative magnetic anomalies, respectively.

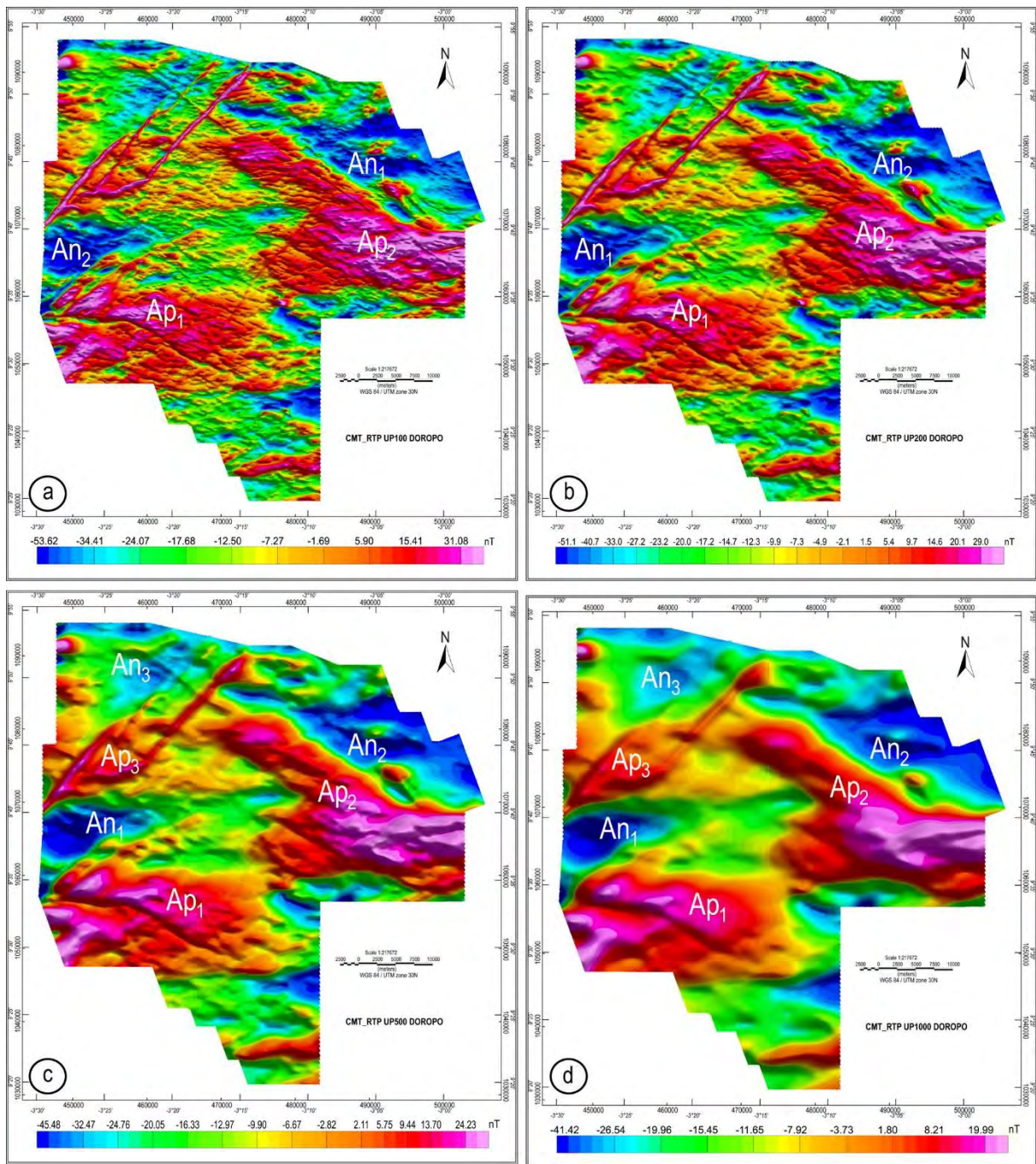


Fig. 11. Upward continuation maps at (a) 100 m, (b) 200 m, (c) 500 m and (d) 1000 m. Same notations as in Fig. 10.

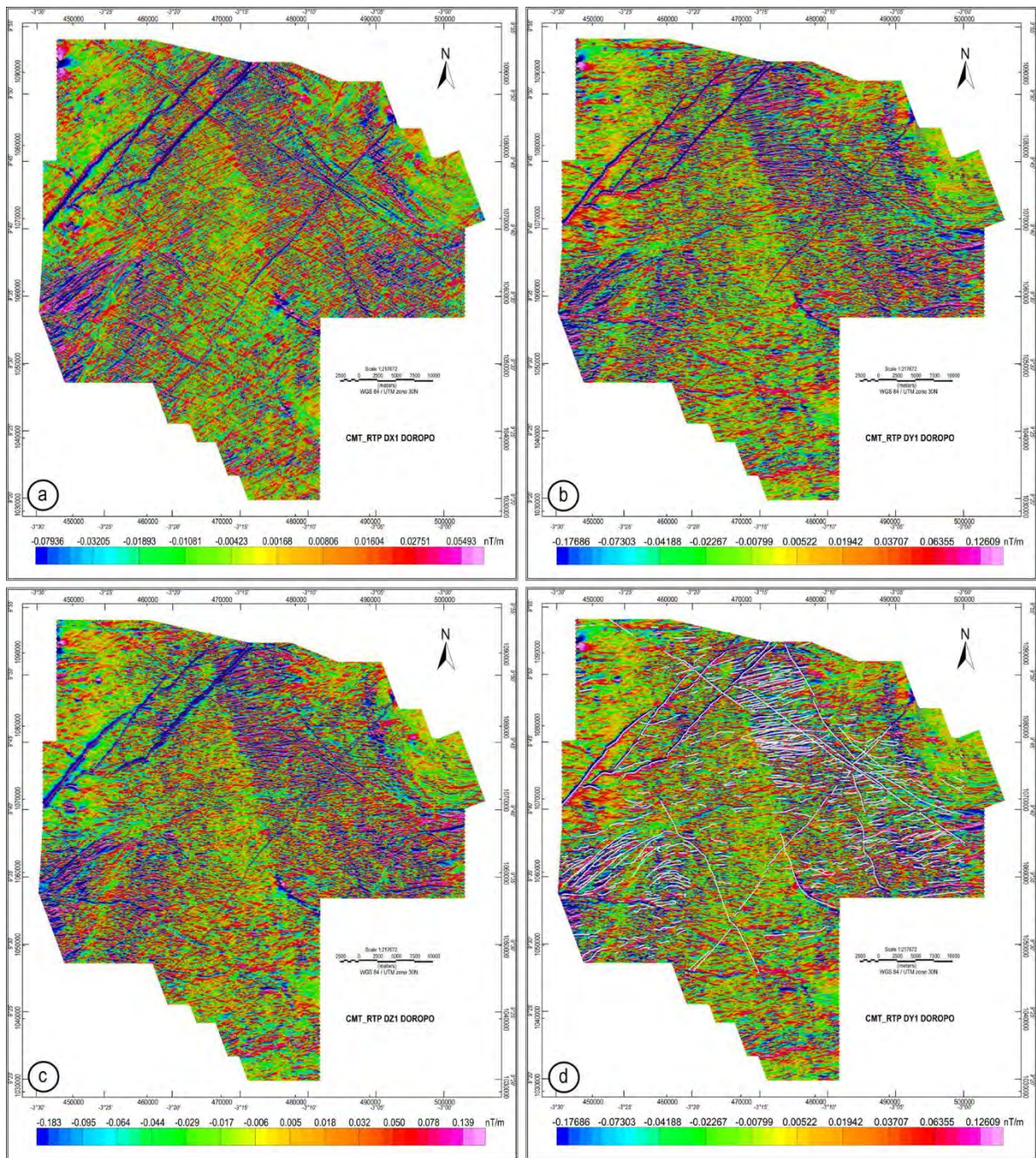


Fig. 12. Gradient maps according to (a) X; (b) Y; (c) Z and (d) Structural sketch related to faults, shears, dykes and magnetic lineaments superimposed on the derivative map according to Y.

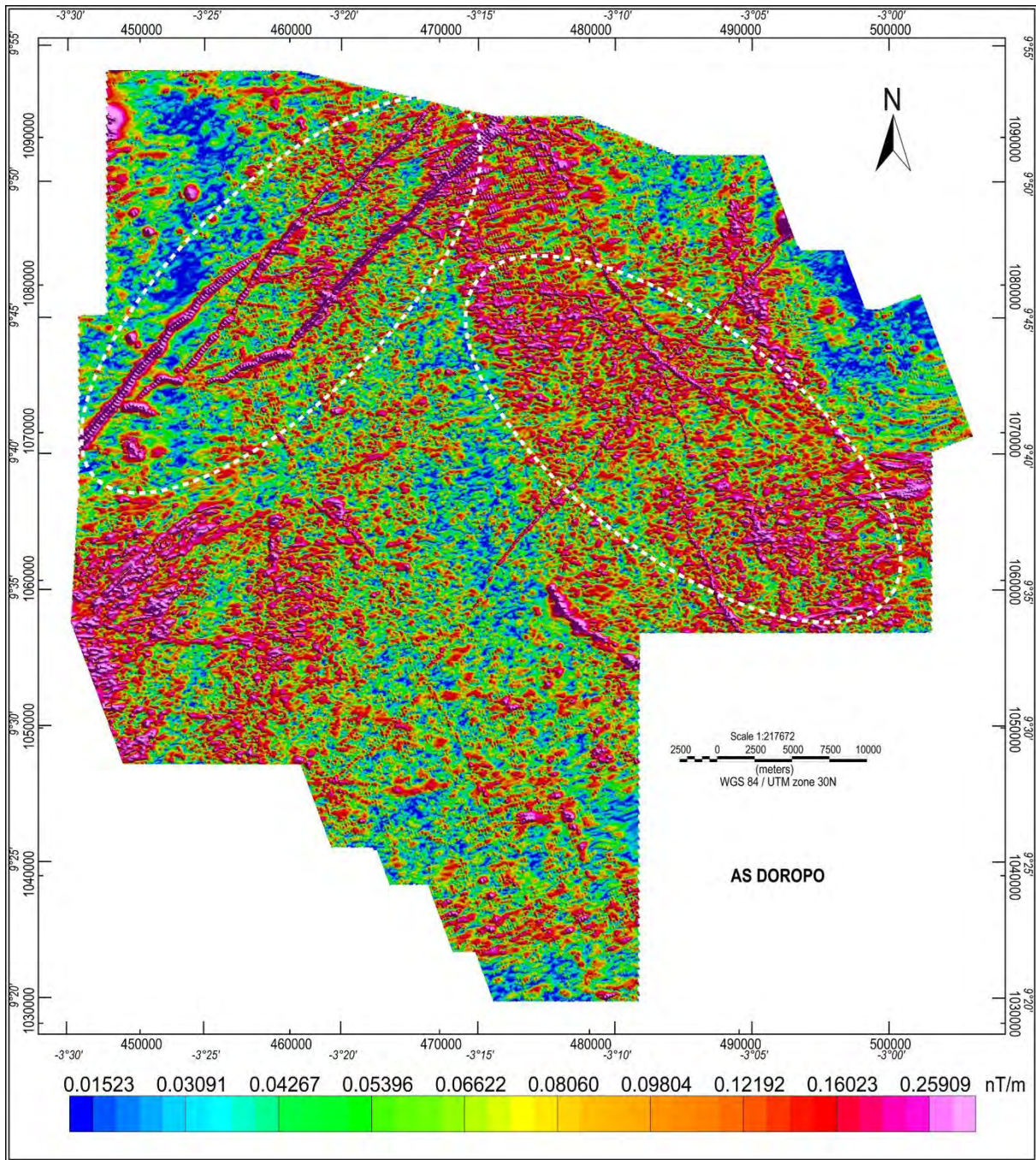


Fig. 13. Analytical signal map showing geological bodies of the same nature. Areas within the white dotted lines show NW-SE and NE-SW oriented structures.

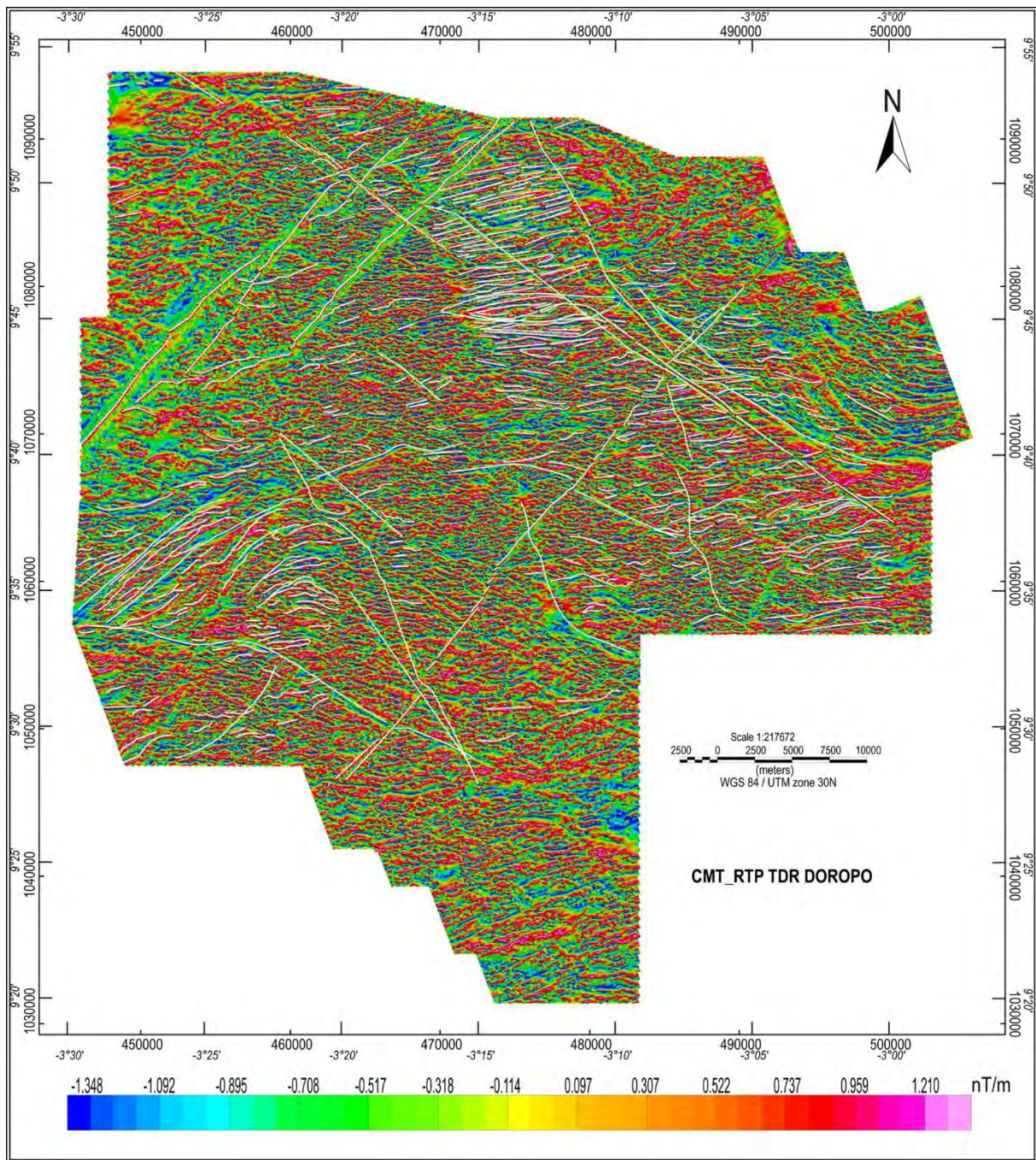


Fig. 14. Map of the Tilt Derivative showing linear (faults, shears) and massive structures with curvilinear magnetic lineaments (white lines).

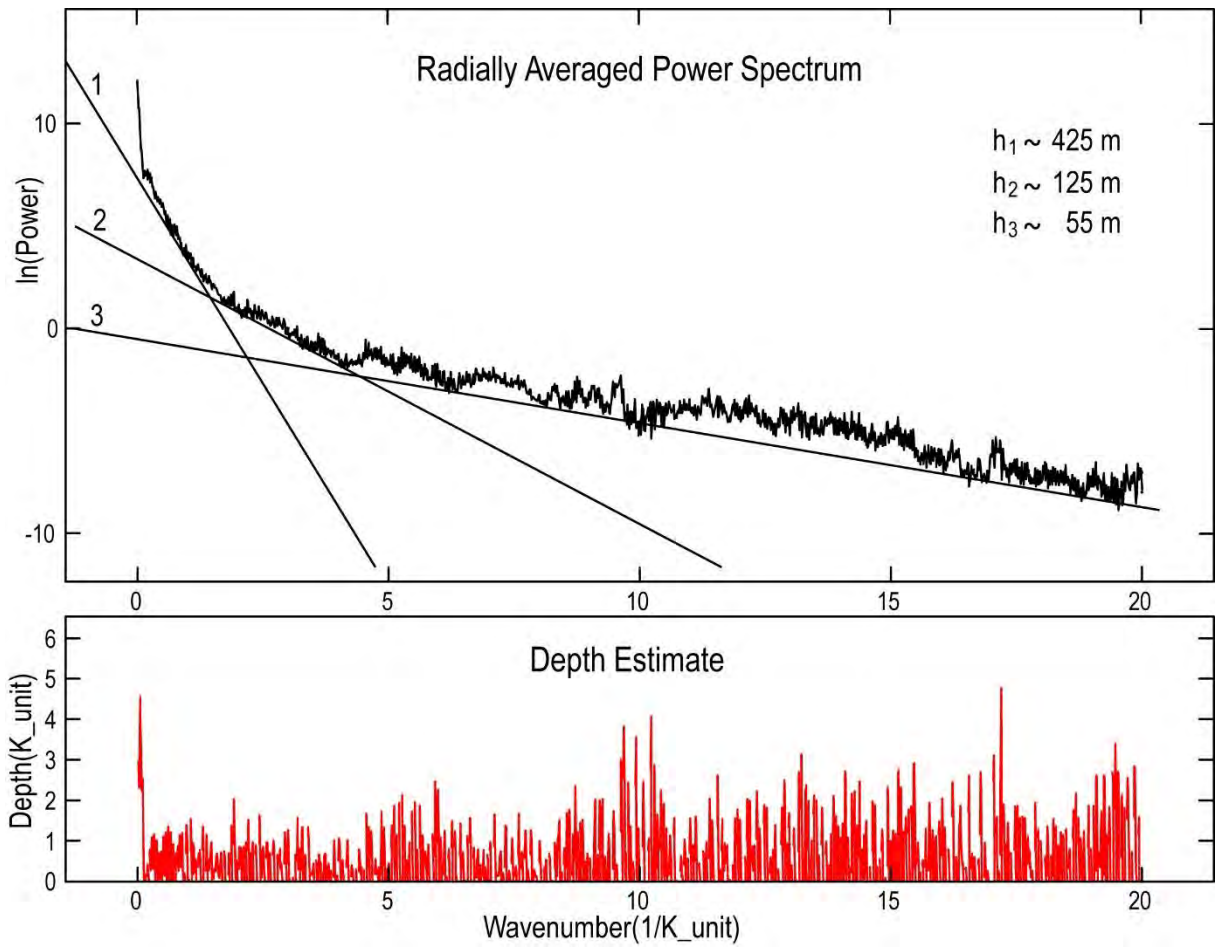


Fig. 15. Power spectral diagram (Spector and Grant, 1970) showing three possible depths of the causative sources at 55 m, 125 m and 425 m.

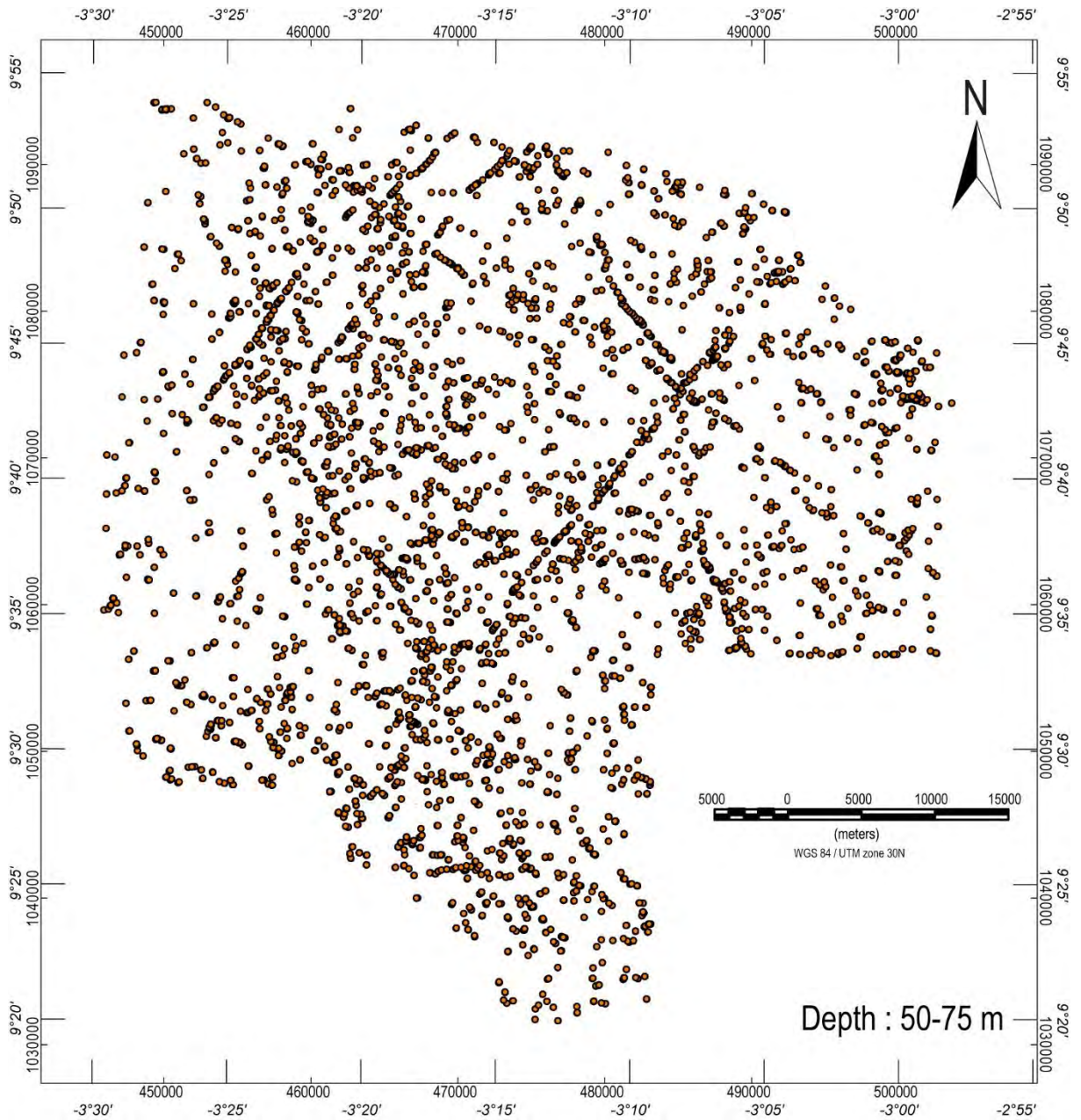


Fig. 16a. Map of the 3D Euler deconvolution solutions for depth plans in the ranges 50-75 m: shows NE-SW and NW-SE oriented linear structures;

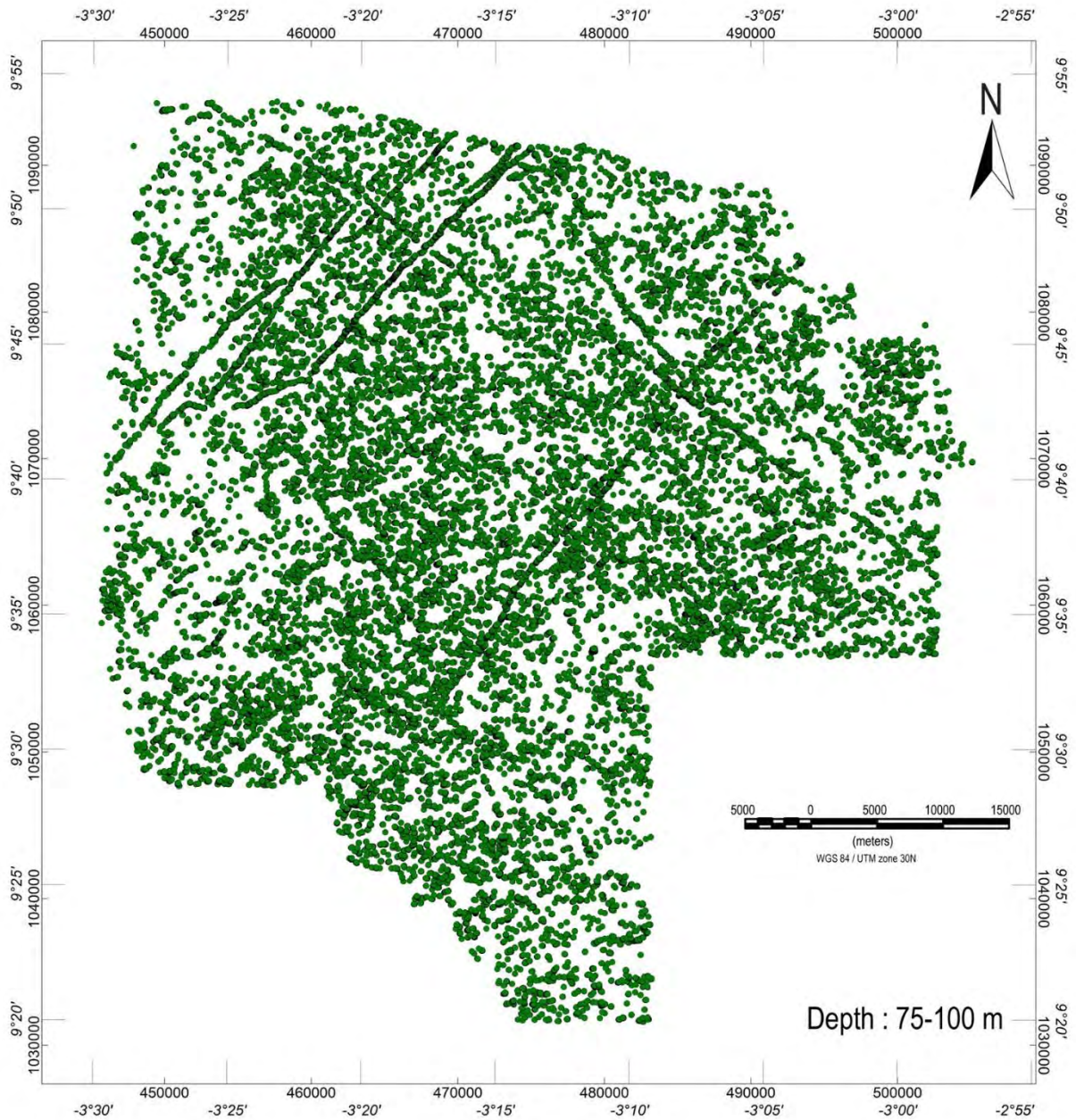


Fig. 16b. Map of the 3D Euler deconvolution solutions for depth plans in the ranges 75-100 m: highlights the same linear structures as in Fig. 16a.

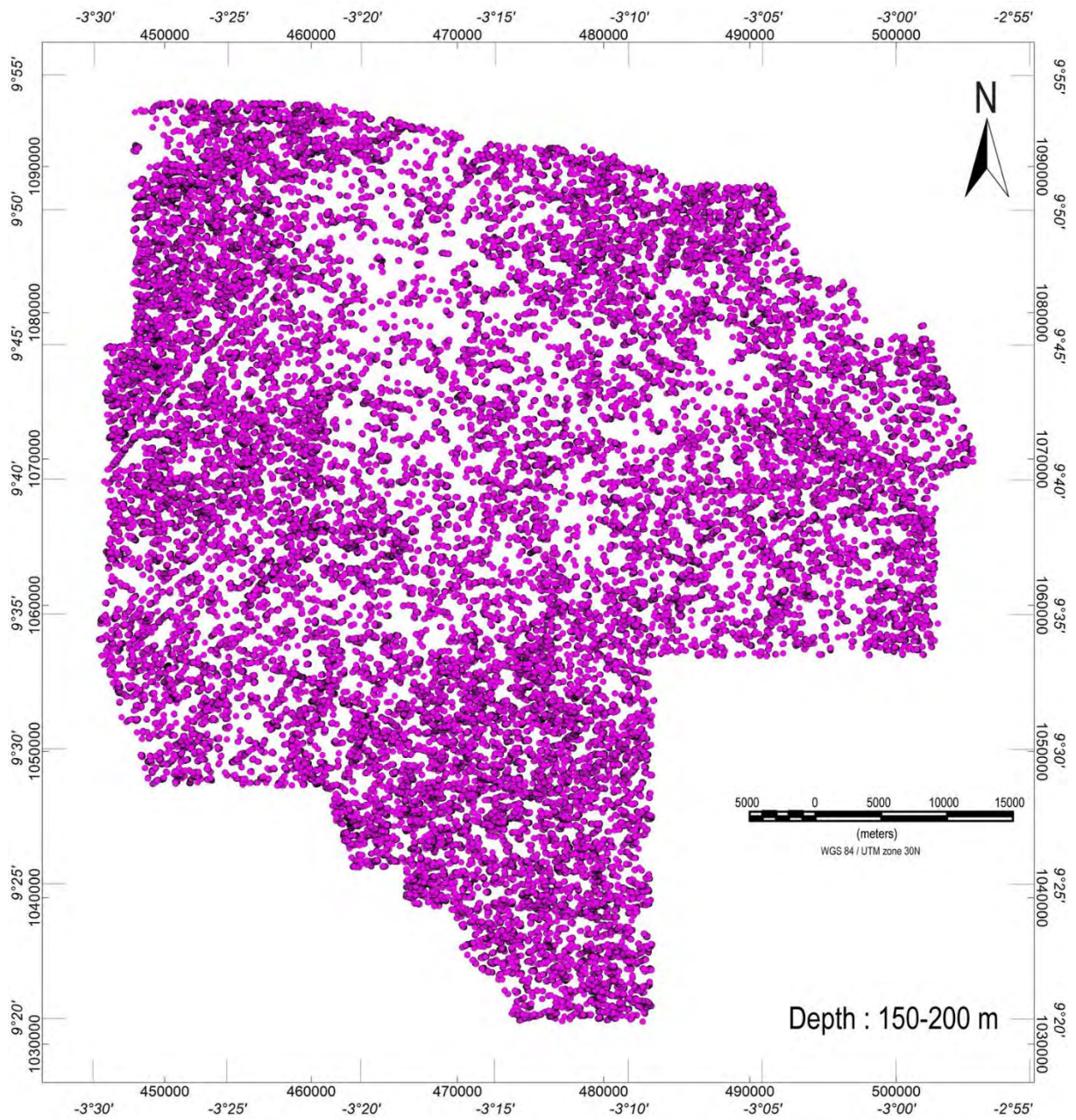


Fig. 16c. Map of the 3D Euler deconvolution solutions for depth plans in the ranges 150-200 m: the linear structures tend to disappear except some NE-SW structures (e.g., northwestern the map).

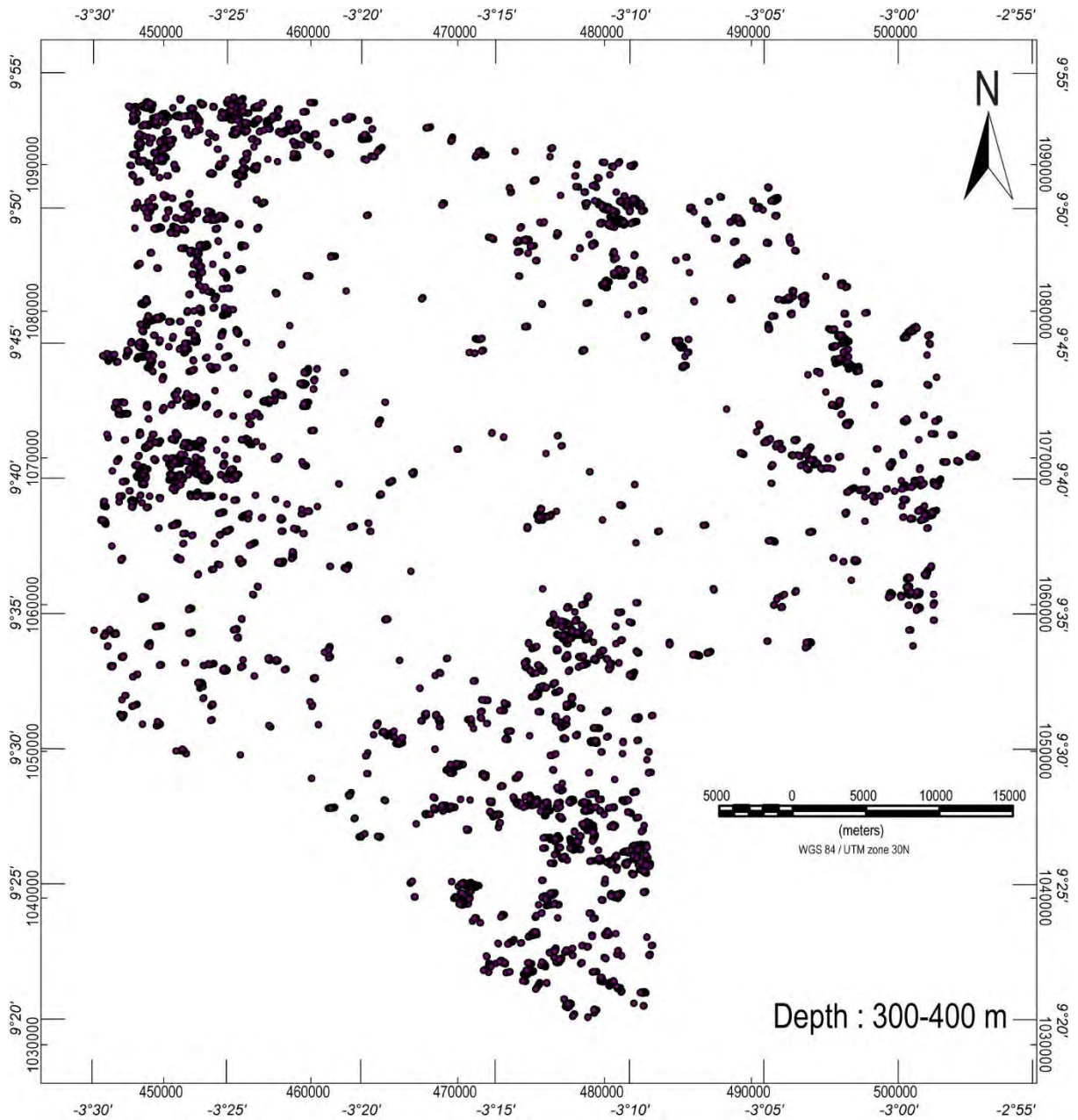


Fig. 16d. Map of the 3D Euler deconvolution solutions for depth plans in the ranges 300-400 m: all linear structures disappeared.

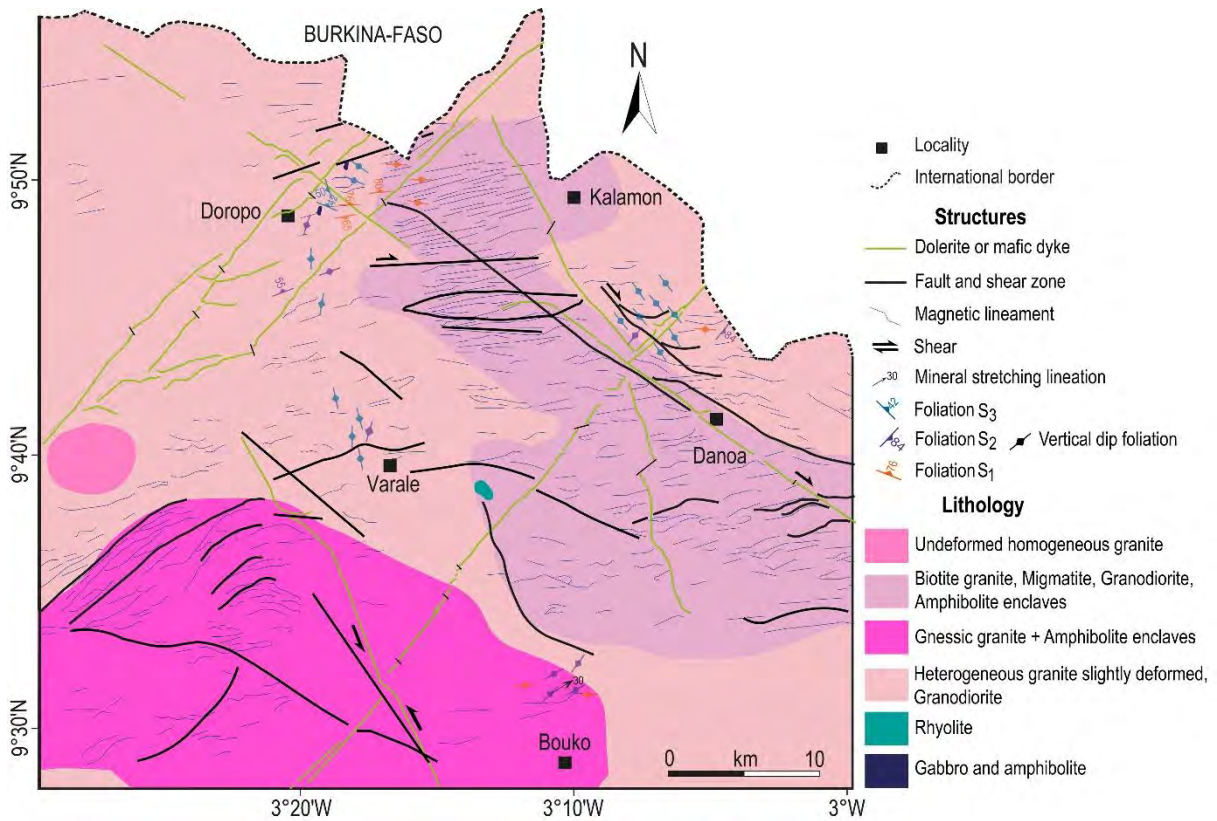


Fig. 17. Lithostructural map of the Doropo region (reduction of the 1:50,000 scale map).

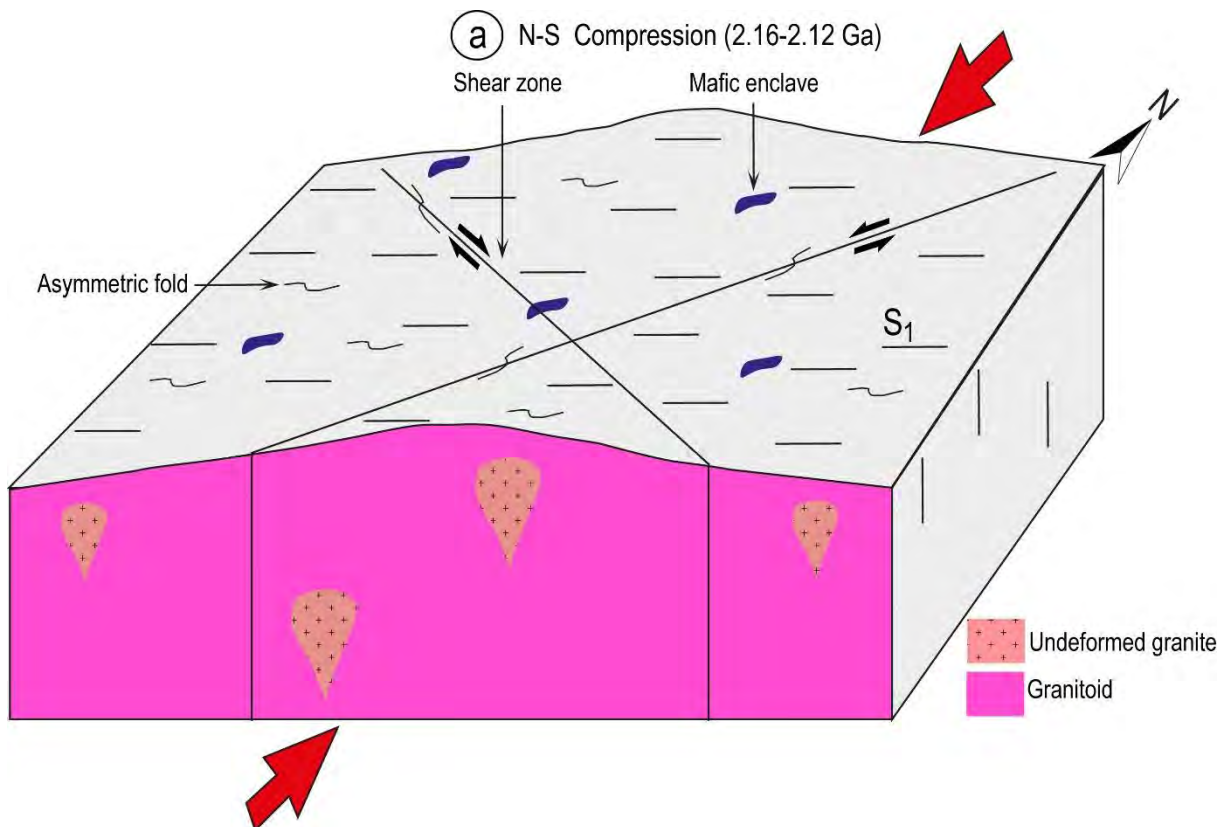


Fig. 18a. Tectonic model proposed for the Doropo region during the Eburnean. Crustal thickening and emplacement of granitoids. Red arrow indicates the σ_1 direction.

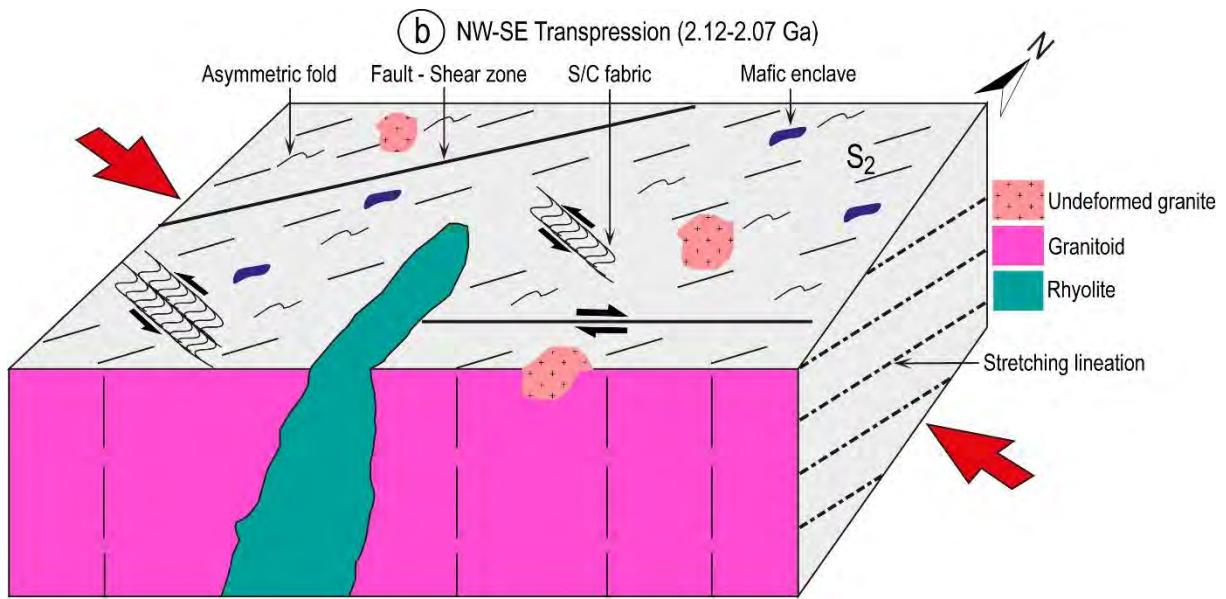


Fig. 18b. Tectonic model proposed for the Doropo region during the Eburnean. Occurrence of oblique shears.

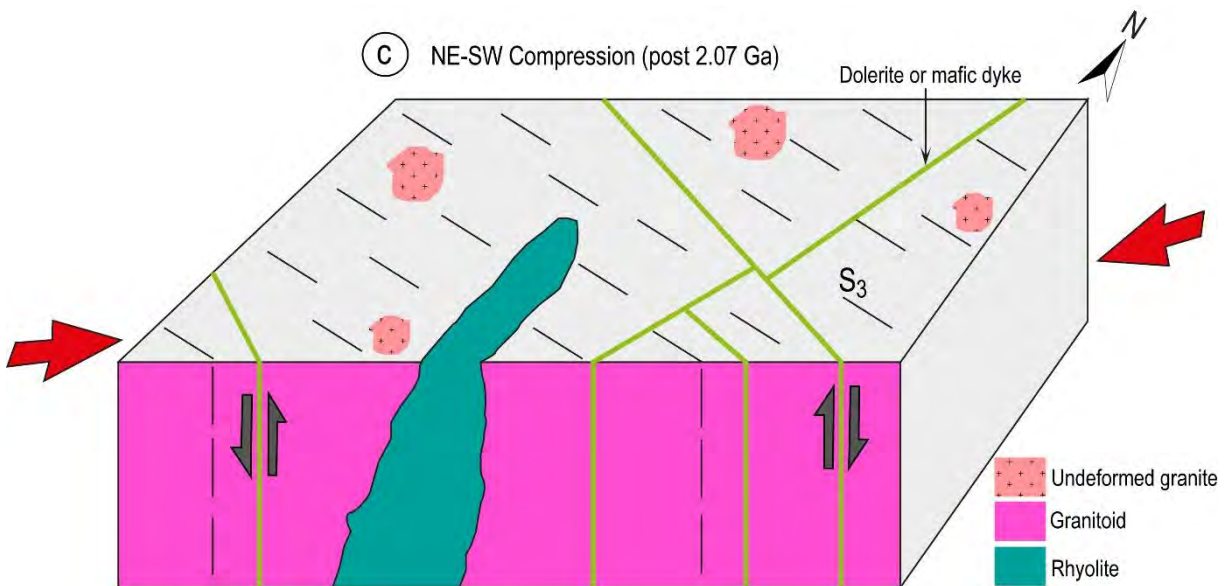


Fig. 18c. Tectonic model proposed for the Doropo region during the Eburnean. reactivation of faults and magmatic inflows.